



# The impact of model resolution on the North Atlantic response to anthropogenic aerosols

Wah Kin Michael Lai<sup>1</sup>, Jon Robson<sup>2</sup>, Laura Wilcox<sup>2</sup>, Nick Dunstone<sup>2</sup>, and Rowan Sutton<sup>1,2</sup>

<sup>1</sup>Met Office Hadley Centre, Exeter, U.K.

<sup>2</sup>National Centre for Atmospheric Science, University of Reading, Reading, U.K.

**Correspondence:** Wah Kin Michael Lai (michael.lai@metoffice.gov.uk)

**Abstract.** A set of novel, idealised, single-forcing experiments were performed to isolate the impact of anthropogenic sulphur dioxide emissions on North Atlantic SST variability. The medium-resolution (60km atmosphere, 0.25° ocean) and low-resolution (135km atmosphere, 1° ocean) of the HadGEM3-GC3.1 model were used to investigate the impact of resolution on the forced response. The SST response at both resolutions is timescale dependent: a fast, large-scale surface cooling is 5 followed by a slow, ocean-driven warming responses. Warming of the sub-polar North Atlantic is due to a strengthening of the Atlantic Meridional Overturning Circulation (AMOC) and is stronger at the medium resolution. This difference is related to surface density fluxes across the subpolar North Atlantic. The growth of Labrador Sea ice is stronger at low-resolution which inhibits air-sea interaction and reduces surface buoyancy forcing, leading to a weaker AMOC response. There is also evidence of a stronger AMOC positive feedback involving salt-advection at medium-resolution. These results show that the large-scale 10 North Atlantic response to external forcing can be sensitive to regional differences, such as model climatology of Labrador Sea ice and its response to aerosol cooling.

*Copyright statement.* The works published in this journal are distributed under the Creative Commons Attribution 4.0 License. This licence does not affect the Crown copyright work, which is re-usable under the Open Government Licence (OGL). The Creative Commons Attribution 4.0 License and the OGL are interoperable and do not conflict with, reduce or limit each other. ©Crown copyright 2025, Met 15 Office.

## 1 Introduction

In observational records, the North Atlantic basin has been through decades of warm and cold phases relative to the rest of the world. This slow variation in North Atlantic sea surface temperature (SST) is referred to as the Atlantic Multidecadal Variability (AMV, Sutton et al. (2018)) and has far-reaching impacts on the global climate system. AMV influences include 20 summer conditions in western Europe, precipitation across the eastern US, Atlantic hurricanes and tropical precipitation around the world (Sutton and Hodson, 2005; Sutton and Dong, 2012; Ruprich-Robert et al., 2018; Peings and Magnusdottir, 2014; Gastineau and Frankignoul, 2015; Zhang and Delworth, 2006; Wang et al., 2012; Ruprich-Robert et al., 2017; Martin et al., 2014; Monerie et al., 2019). Hence, there is great interest in understanding how the AMV has evolved in the past and how



it may change in the future. However, details of the governing mechanisms remain uncertain. One key outstanding question  
25 is the relative importance of internal unforced variability versus externally forced changes associated with changing levels of  
anthropogenic emissions over the historical period.

Many climate models can spontaneously generate AMV-like variability in the absence of anthropogenic forcing, i.e. in control simulations (Ba et al., 2014; Kim et al., 2018; Wills et al., 2019). This unforced internal AMV is typically driven by changes in the Atlantic Meridional Overturning Circulation (AMOC) and associated heat transport (Bjerknes, 1964; Knight, 30 2005; Delworth and Mann, 2000; Wills et al., 2019; Lai et al., 2022). However, internally simulated AMV usually has significant deficiencies in time scale, magnitude, and spatial pattern (Cheung et al., 2017; Peings et al., 2016). The inclusion of external forcing, i.e. historical simulations, have been argued to better capture the pattern and timescale of AMV, leading to the hypothesis that varying levels of anthropogenic forcing have played a major role in the observed AMV (Booth et al., 2012; Bellomo et al., 2018; Bellucci et al., 2017; Watanabe and Tatebe, 2019). The emissions of anthropogenic sulphate aerosols 35 from North America and Europe during the industrial period have been highlighted as a particularly important driver of the observed AMV (Booth et al., 2012).

Details of the mechanism linking anthropogenic aerosols (AA) to North Atlantic SST changes remain unanswered. On the one hand, Booth et al. (2012), showed that aerosol forced changes project onto the AMV pattern through modulation of incoming solar radiation by interacting with climatological winds and clouds. Although the strength of aerosol forcing has been 40 shown to be too large in the model used in the Booth study (Zhang et al., 2013), many subsequent studies with other models have shown similar links between anthropogenic aerosol forcing and North Atlantic SST (Undorf et al., 2018; Watanabe and Tatebe, 2019; Bellomo et al., 2018). On the other hand, some studies have argued that AA can have a delayed impact on North Atlantic SST through a forced strengthening of the AMOC caused by the initial surface cooling, which then leads to a delayed warming of the North Atlantic (Menary et al., 2013, 2020; Robson et al., 2022; Hassan et al., 2021). Furthermore, the 45 modulation of the radiative budget is not the only way AA can drive SST changes; turbulent heat flux changes can be driven by the advection of cold, dry air from the continents instead (Robson et al., 2022).

Many of the mentioned studies are based on historical simulations, making it difficult to disentangle specific mechanisms because of the competing influences from many different sources of forcing. Furthermore, there is large model diversity in the representation of both the internal (Wills et al., 2019), and historical AMV (Han et al., 2016). This study aims to address 50 these two modelling issues, namely the difficulty in disentangling the physical processes and model diversity, in the context of understanding the mechanisms governing externally forced Atlantic variability. A better understanding of the mechanisms governing North Atlantic SST changes, and the physical processes explaining model differences can help us better understand the observational records which will lead to improvements in modelling and better predictions of the climate impacts associated with North Atlantic variability in the coming decades.

55 To address the first question, a set of idealised, single-forcing experiments is designed to isolate the processes linking AA to the North Atlantic SST changes. To address the second question, these single-forcing experiments are performed using the medium-resolution (MM) and low-resolution (LL) versions of the HadGEM3-GC3.1 model. This set of experiments will also explore whether the differences in forced changes are consistent with differences in the mechanisms driving unforced changes.



A previous study has shown that both models simulate internal AMV, but the mechanisms driving it are different, with a bigger  
60 role for the winter NAO in the MM model (Lai et al., 2022). Additionally, because the processes governing the subpolar and  
subtropical AMV can be different (Lai et al., 2022), this study will consider the processes driving the two regions separately.

This study is organised as follows. The design of the idealised single-forcing experiment is first presented in section 1.1.  
An evaluation of the aerosol's impact on surface and top-of-atmosphere radiation is then presented in section 1.2. The overall  
65 response of the SST and the role of surface fluxes are explored in 2.1 and 2.2. Following this, section 2.3 will investigate  
the ocean heat transport response and AMOC response. A detailed analysis into the differences in surface buoyancy flux is  
presented in section 2.4. Finally, section 3 contains a summary and discussion of the key findings of this study.

## 1.1 Model used and experiment design

### 1.1.1 The HadGEM-GC3.1 model

The HadGEM3-GC3.1 coupled model used in this study forms part of the UK Met Office's contribution to CMIP6 simulations  
70 (Eyring et al., 2016). Relative to HadGEM2-AO, which was the Met Office's submission to CMIP5, the HadGEM3-GC3.1  
model includes new ocean and sea ice models, new aerosol and cloud schemes, major revisions to the atmosphere dynamical  
core and many more updates to the parametrisation schemes. These revisions have led to marked improvements in many  
aspects of the simulated present-day climate. Detailed comparisons between the HadGEM3-GC3.1 model and its predecessors  
are given by Williams et al. (2018).

75 HadGEM3-GC3.1 is comprised of: a global atmosphere-land configuration GA/GL7.1 (Walters et al., 2019), with a new  
modal aerosol scheme (GLOMAP mode, Mulcahy et al. (2020)); a global ocean component GO6 (Storkey et al., 2018) based  
on version 3.6 of the Nucleus for European Modelling of the Ocean (NEMO) ocean model Gurvan et al. (2017); a sea ice  
model configuration GSI8.1 (Ridley et al., 2018); and finally, coupling between the ocean and atmosphere models are handled  
by the OASIS-MCT coupler (Valcke et al., 2015), with a coupling period of 1 hour.

80 The two versions of the model used throughout this study are denoted LL and MM (known as HadGEM3-GC3.1-LL  
and HadGEM3-GC3.1-MM, respectively, in CMIP6 nomenclature). The medium-resolution (MM, N216-ORCA025) model  
(Williams et al., 2018) has horizontal resolution of 60 km in the mid-latitude atmosphere and 0.25° in the ocean. The low-  
resolution (LL, N96-ORCA1) model (Kuhlbrodt et al., 2018) has horizontal resolution of 135 km in the atmosphere and 1° in  
the ocean. The vertical resolution is the same in both models, with 85 pressure levels in the atmosphere, up to 85 km, and 75  
85 depth levels in the ocean.

A top priority during the development of the HadGEM3-GC3.1 models was to minimise the dependence of parameters on  
model resolution. This has the benefit of helping to understand the effect of model resolution on important climate process.  
Therefore, the MM and LL models are extremely similar and differ mainly in horizontal resolution. However, there are still  
90 some small physical differences between LL and MM, which arise mainly from the use of different parameter values to  
compensate for resolution-dependent processes. For example, the LL atmosphere has different parameter values to compensate  
for lower maximum winds and limited resolution of gravity wave drag. There are also differences in the ocean submodels;



in particular, ORCA1 includes a Gent–McWilliams parameterisation for eddy-induced fluxes but ORCA025 does not, and ORCA1 also has a slightly lower albedo for snow on sea ice to compensate for weak Arctic sea ice bottom melt. Further details and a summary table of the differences are included in Kuhlbrodt et al. (2018).

### 95 1.1.2 Experimental design

To investigate and isolate the influence of historical AA emissions on the North Atlantic, a set of idealised single-forcing experiments is performed. The forcing applied is realistic in spatial pattern and magnitude, but idealised in time. A perturbation of only sulphur dioxide ( $\text{SO}_2$ ) emissions are introduced to otherwise pre-industrial (PI) conditions. These emissions are based on the CMIP6 historical emissions within the North Atlantic sector (i.e. North American and European emissions). The spatial 100 pattern of the minimum (1850) and maximum (1973)  $\text{SO}_2$  emissions are shown in figure 1a & b. The timescale of how these emissions are applied in the experiment is shown in figure 1d. The experiment begins from PI conditions,  $\text{SO}_2$  emissions then ramp-up linearly for the first 10 years up to a maximum rate of 1700 kg/s (defined as the 15-year mean around 1973). The maximum emission rate is then held constant for 20 years, before ramping back down to PI conditions over 10 years. The simulation ends with 10 years of constant forcing at PI conditions, running a total of 50 years.

105 The reason for considering only  $\text{SO}_2$  emissions (while omitting organic carbon, black carbon and dust) is because sulphate aerosol is the primary agent of AA radiative forcing during the historical period (Thornhill et al., 2021) and previous studies have found that multidecadal changes in  $\text{SO}_2$  emissions have had the greatest influence on North Atlantic SST changes (Booth et al., 2012; Chang et al., 2011). The purpose of this set of experiments is to identify the specific mechanism linking these  $\text{SO}_2$  emissions to the AMV, without the influence of competing sources of external forcing.

110 Asian  $\text{SO}_2$  emissions are not considered and only emissions from the North Atlantic sector are included in this experiment for the same reason; to simplify the situation and help isolate specific mechanisms. This is because the processes linking emissions from different regions to the North Atlantic are likely different. For example, North American and European aerosols do so predominantly through local short-wave changes (Booth et al., 2012; Chang et al., 2011), but Asian aerosols may affect the North Atlantic through complex teleconnection mechanisms (Wilcox et al., 2019), with potentially competing effects.

115 The timescale and magnitude of the idealised  $\text{SO}_2$  emissions are chosen to simulate the multidecadal timescale of the historical  $\text{SO}_2$  emissions. Timeseries of the historical  $\text{SO}_2$  emissions across the North Atlantic sector are shown in figure 1c. The ramping-up and ramping-down of emissions in the idealised perturbation is designed to simulate the rapid rise and fall of emissions from the 1930s to the present day. Because the peak emissions of North America slightly leads the European emissions peak, a 15-year mean around 1973 captures the peak emissions of both regions and is therefore used as the maximum 120 emission rate for the idealised perturbation. The idealised time series is useful for identifying key processes, because the projection of such a distinctive timeseries on different variables shows clear links between how different variables influence each other. In addition, seasonal cycles to the emissions are not considered in the single-forcing experiment, the emission ramp-up occurs at each monthly timestep of the model simulations.

125 This set of experiments is different to the Detection and Attribution Model Intercomparison Project (DAMIP, Gillett et al. (2016)) and Precipitation Driver Response Model Intercomparison Project (PDRMIP, Myhre et al. (2017)) experiments per-



formed as part of CMIP6. The DAMIP experiment includes single-forcing simulations, however, global emissions are used and the emissions follow the historical timeseries, making it more difficult to isolate specific mechanisms linking AA and North Atlantic changes. The PDRMIP experiment is more similar to our set of idealised experiments, including single-forcing simulations with additional regional emission simulations and idealised temporal evolution. However, the PDRMIP idealised 130 temporal evolution is designed to test equilibrium responses instead of simulating historical changes and the regional emissions are Europe-only or Asia-only. Lastly, for the PDRMIP simulations, the ocean outputs were not archived.

## 1.2 TOA energy imbalance

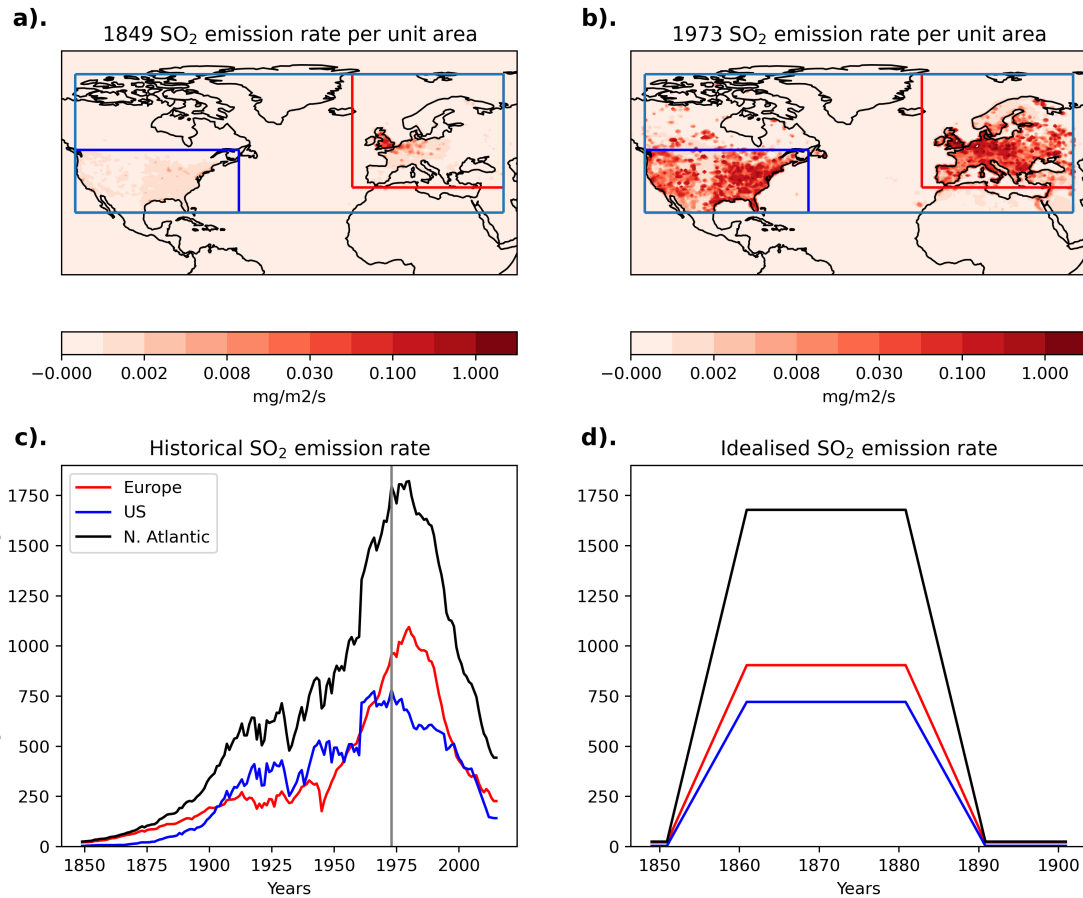
The overall effect of the aerosol emission on spatial distributions of aerosol optical depth (AOD), total cloud fraction and its impact on the radiative effects at the top-of-atmosphere (TOA) and at the surface are shown in figure 2. Changes in AOD gives 135 an indication to the aerosol-radiation-interactions (ARI) and total cloud fraction shows how the spatial distribution of clouds change. A caveat here is that total cloud fraction only reflects one aspect of cloud changes and therefore does not reflect the full aerosol-cloud-interactions (ACI). For example, the Twomey effect (i.e. increased reflectivity of cloud, (Twomey, 1977) is not captured. However, the focus of this study is to understand the influence of aerosol on the climate rather than focus on individual aerosol processes. We then assess the total amount of aerosol-forced radiative changes by investigating the responses 140 in the net top-of-atmosphere shortwave radiation (TOA SW) and net surface downward short wave radiation (DWSW). For both TOA SW and DWSW, positive (red) indicates downward anomalies and negative (blue) indicates upward anomalies.

Figure 2a & d shows that the increase in  $\text{SO}_2$  emissions results in an increase in AOD over the North Atlantic sector. Due to the short lifetime (3-7 days, Rasch et al. (2000)) of tropospheric sulphate aerosols, the largest AOD anomalies are located over the main emission regions; western Europe and the east coast of America. There are also weak AOD anomalies over the North 145 Atlantic ocean and the Eurasian continent which are downstream of the emission regions, indicating advection of aerosols.

The  $\text{SO}_2$  emissions also induce an increase in total cloud fraction across much of the globe in both models (fig. 2b & e). The largest increases in total cloud fraction are over the source regions. Outside of the source regions, there are also large and significant increase of total cloud fraction over the North Atlantic ocean and the Pacific ocean. There is a reduction of cloud 150 fraction over India in both models, which is consistent with previous studies that show a weakening of the Indian monsoon in response to anthropogenic sulphate aerosol changes (Guo et al., 2016).

The timeseries in figure 2g & h, shows that the increase in AOD and total cloud fraction is consistent with the reduction in the total amount of solar radiation absorbed by the Earth, shown by negative anomalies in the TOA SW (fig. 2c & f). Both models show strong negative TOA SW anomalies across the whole Northern Hemisphere, and weak anomalies across the Southern Hemisphere. The largest TOA SW anomalies are located over the aerosol source regions, and the Arctic sea ice 155 regions. Outside of these two regions over the Pacific and Atlantic oceans, negative TOA SW anomalies are co-located with increased total cloud fraction, indicating the importance of the cloud response in governing the overall energy imbalance.

A more quantitative comparison of the total aerosol forcing between the two models is shown by the time series in figure 2i. Since the aerosols are only emitted in the Northern Hemisphere, the interhemispheric difference of the total amount of absorbed solar radiation gives a measure of the strength of the aerosol forcing (Menary et al., 2020) and also an indicator for how strong



**Figure 1.** Spatial pattern and time profile of the applied idealised SO<sub>2</sub> emissions. Panel a). shows the pattern of annual mean SO<sub>2</sub> emissions at year 1849, used as minimum emissions for the experiment. Panel b). shows the pattern of annual mean SO<sub>2</sub> emissions at year 1973, used as maximum emissions for the experiment. Note the non-linear colour bars. The black box indicates the North Atlantic sector. Only emissions within the black box are considered for the idealised experiment. The blue and red boxes bound the North America and European domains respectively. Panel c). shows the time series of regional mean historical SO<sub>2</sub> emission rates in the North Atlantic sector (black), North America (blue) and Europe (red). These three regions correspond to the regions marked in panels a). and b). Panel d). shows the time series of the idealised SO<sub>2</sub> emission rates used in the experiments.

160 the AMOC is likely to be, since the AMOC will act to restore this interhemispheric imbalance (Robson et al., 2022). Anomalies pole-wards of 60°N and 60°S are not considered to remove influences due to the sea ice response. The time series are smoothed by a 5-year running mean to minimise the year-to-year variability.

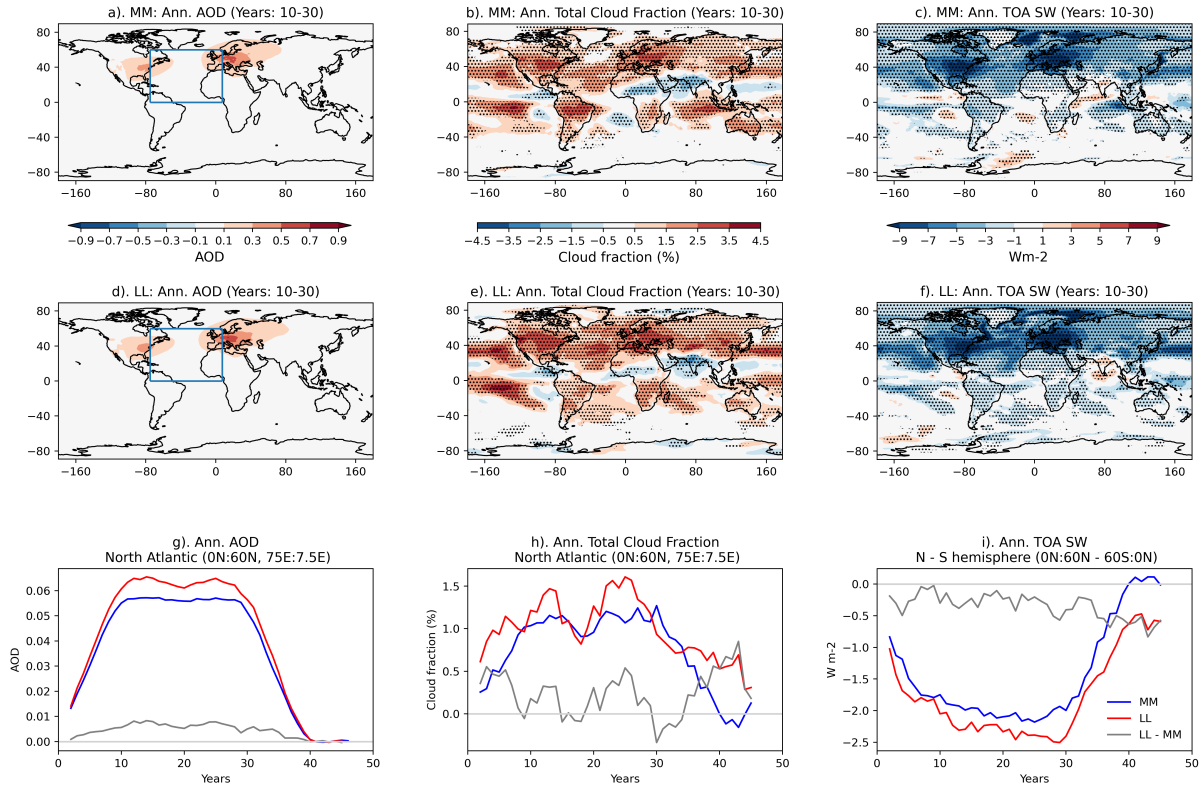


**Figure 2.** Spatial pattern and timeseries of the forced changes in aerosol optical depth (AOD), total cloud fraction and top-of-atmosphere net downward shortwave radiation (TOA SW). Panel a). shows spatial pattern of anomalous AOD averaged across years 10-30 of the forced simulation for the MM model. Panel b). shows the same as a). but for total cloud fraction. Panel c). shows the same as a). but for TOA SW. Stippling indicates where the response is significant at the 10% level, based on a two-tailed Student's t-test. Panel d), e), and f) shows the same as a), b), and c) but for the LL model. Panel h). shows the timeseries of area-averaged annual-mean aerosol optical depth (AOD) taken across the North Atlantic basin ( $0^{\circ}\text{N}$  to  $60^{\circ}\text{N}$ ,  $7.5^{\circ}\text{E}$  to  $75^{\circ}\text{E}$ ). Panel i). shows the same as h). but for the total cloud fraction instead of AOD. Panel j). shows the interhemispheric difference ( $0^{\circ}\text{N}$  to  $60^{\circ}\text{N}$  minus  $0^{\circ}\text{S}$  to  $60^{\circ}\text{S}$ ) in downwards top-of-atmosphere net shortwave radiation (TOA SW) for the MM model (blue) and the LL model (red). The difference between the two models are shown in grey. All timeseries are smoothed by a 5-year running mean.

At both the surface and at the top of the atmosphere, the magnitude of the interhemispheric energy imbalance is greater in the LL model, by around  $0.25\text{Wm}^{-2}$  (fig. 2i). This stronger forcing is related to both larger AOD perturbations and a stronger cloud response over the North Atlantic ocean (fig. 2g, h). The specific aerosol processes at play are not the focus of this study.



## 2 Results

### 2.1 SST response

We begin the analysis by looking at the evolution of SST in response to the aerosol forcing before investigating the mechanisms which control these SST changes in later sections.

170 Figure 3 shows the evolution of annual mean SST. The overall evolution of SST is similar between the two models. In both models, there is an initial (years 0-4) cooling across the North Atlantic. North hemisphere SST continues to cool as SO<sub>2</sub> emissions reach its maximum (years 12-16). This cooling is especially large in the sea ice regions, in the Barents and GIN Seas in both model and also the Labrador Sea in the LL model. However, the subpolar North Atlantic (SPNA) evolves differently to the rest of the basin. The SPNA becomes anomalously warm starting from years 16-20, and the warm anomalies 175 continue to strengthen and persist to the end of the experiment. From year 38-42, the spatial pattern and magnitude of the SPNA warm anomalies are different between the two models. In the MM model, there are warm anomalies along the Gulf Stream extension region and in the central SPNA. In the LL model, the warm anomalies are weaker and lie only over the central SPNA. (Importantly, the interplay between the fast cooling, and slow SPNA warming creates a disconnection between the SPNA and subtropical NA, which is not consistent with the observed AMV pattern which instead shows a coherent, basin-180 wide variation in SST (Sutton et al., 2018). This indicate that in this model, the historical AMV is not mainly forced by changes in anthropogenic SO<sub>2</sub> emissions.)

The following subsections will explore in detail, the mechanisms driving the SST changes. We will first examine the role of surface fluxes, and the processes controlling these fluxes. We will then assess the role of forced ocean circulation changes. Specifically, we will look at the processes linking aerosol emissions to AMOC changes and how these differ between the two 185 resolutions.

### 2.2 Role of surface heat fluxes

As mentioned in the introduction, there are two sets of proposed mechanisms linking aerosol forcing to SST changes in the literature, one is driven by surface heat fluxes (Booth et al., 2012), and the other by forced ocean circulation changes (Menary et al., 2020). Therefore, the following analysis will first focus on the role of surface heat fluxes, and the relative importance of 190 radiation versus turbulent heat fluxes (THF).

Section 1.2 has shown that there are indeed significant clouds and surface shortwave changes in both models, we now investigate whether aerosol radiative effects are the primary driver of surface temperature changes as proposed by Booth et al. (2012). We do this by decomposing the annual mean total surface heat flux into contributions from turbulent heat fluxes (THF) and net downward shortwave radiation (DWSW). THF is defined as the sum of latent and sensible heat flux. Changes in 195 the THF is driven by air-sea interactions and can be driven by changes in the atmospheric circulation (i.e. a speeding up or slowing down of surface winds), or can be driven by changes in the air-sea temperature and humidity gradients. Changes in the net DWSW are linked to aerosol radiative effects including both aerosol-radiation interactions (ARI) and aerosol-cloud interactions (ACI). Net DWSW is also sensitive to surface albedo changes, such as from changes in the sea ice. There are

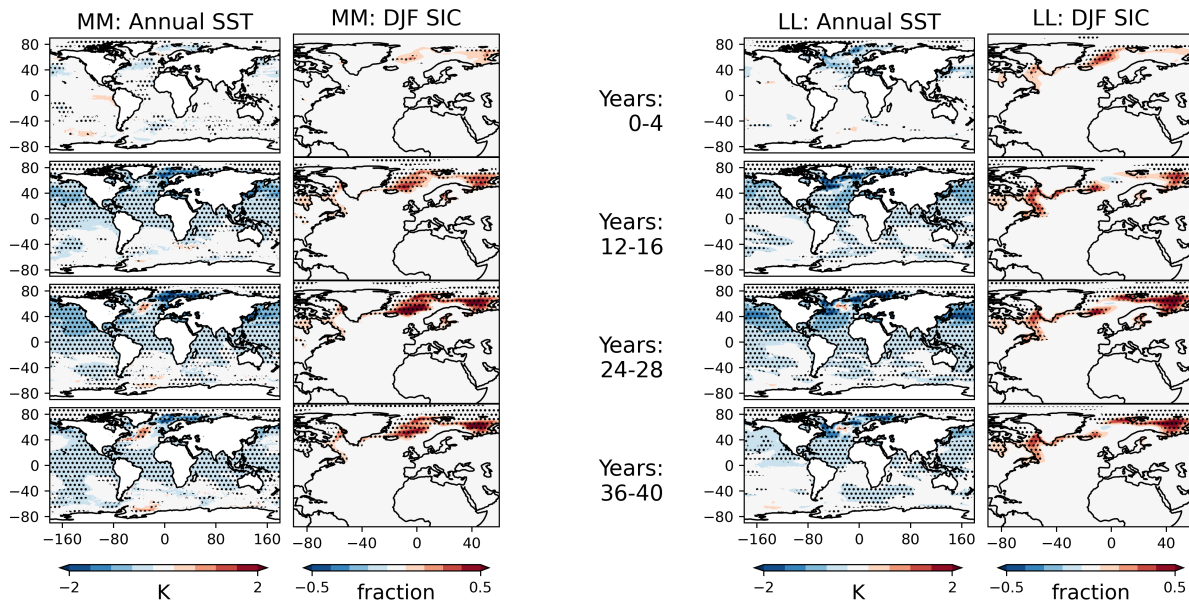


**Figure 3.** Spatial pattern and evolution of the annual-mean, ensemble-mean anomalies of sea surface temperature (SST) and winter (December-January-February, DJF) sea ice concentration (SIC). All variables are smoothed by a 5-year running mean such that Years:0-4 represents the mean value between years 0 and 4. The MM model on the left and the LL model on the right. All variables are smoothed by a 5-year running mean. Stippling indicates where the response is significant at the 10% level, based on a two-tailed Student's t-test.

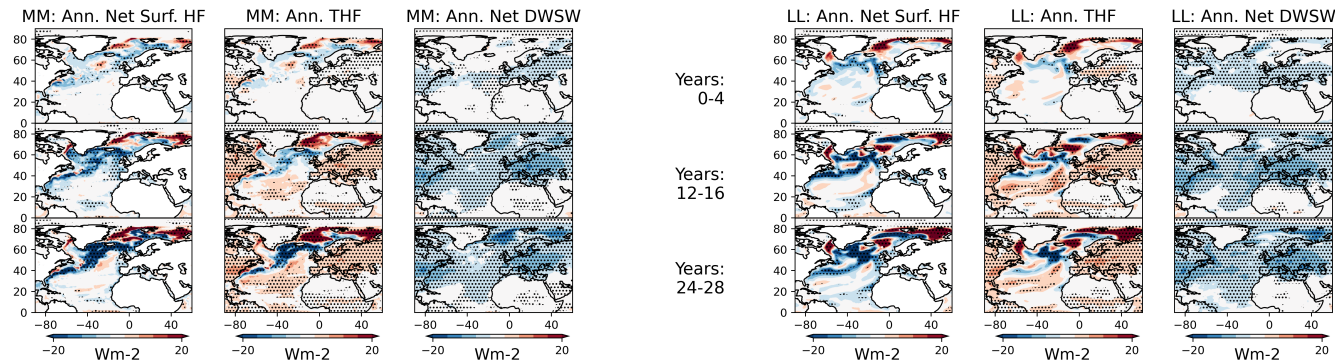
also other terms in the net SHF, such as net downward longwave radiation (DWLW), however, it was found that THF and net  
200 DWSW explained much of the total SHF. DWLW anomalies were the next largest term, but still an order of magnitude smaller  
than DWSW (not shown).

Figure 4 shows the evolution of total surface heat flux alongside the THF and net DWSW components. Both models show  
considerable spatial structure in the total surface heat flux. Initially, the total surface heat flux anomalies are small. As emissions  
205 increase, negative anomalies begin to develop across the subpolar North Atlantic (SPNA). In contrast, positive anomalies  
develop across the Labrador, Nordic and Barents Sea. This pattern of surface heat fluxes is reflected in the THF. Whereas, the  
net DWSW show a much more uniform cooling influence across the whole North Atlantic basin. This difference in spatial  
pattern indicates that it is air-sea interaction, rather than the aerosol radiative effect which is the dominant control of the pattern  
of total surface heat fluxes averaged across the year.

Furthermore, the high latitude positive surface heat flux anomalies can be attributed to sea ice changes. Figure 3 shows the  
210 evolution of winter (December-January-February, DJF) sea ice concentration changes. In both models, the regions of largest  
sea ice growth are co-located with the positive surface heat flux anomalies (fig. 4). This indicate that averaged across the year,  
the dominant effect of sea ice on surface heat fluxes is through its insulating effect rather than its effect on surface albedo.



Whereby, the growth of sea ice covers the ocean surface and inhibits air-sea interaction, resulting in less heat loss than usual. If the sea ice albedo effect was to dominate, then these high-latitude anomalies would be negative instead.



**Figure 4.** Spatial pattern and evolution of the annual-mean, ensemble-mean anomalies of net surface heat flux, turbulent heat flux (THF) and net downward shortwave radiation (DWSW). The MM model on the left and the LL model on the right. All variables are smoothed by a 5-year running mean. Stippling indicates where the response is significant at the 10% level, based on a two-tailed Student's t-test.

## 215 2.3 Ocean heat transport and AMOC changes

The previous section showed that different sections of the North Atlantic appear to respond differently to the aerosol forcing. In particular, surface fluxes on its own does not explain changes in the SPNA SST, i.e. the SPNA SST warms at the same time as strong anomalous surface cooling through THF. Therefore, we now look into the hypothesis that a forced AMOC response may be driving the ocean heat content changes. We first investigate the role of ocean heat transport before comparing the AMOC 220 response between the different resolutions.

The evolution of ocean heat transport (OHT) is shown by the Hovmöller diagrams in figure 5. In both models, northward OHT strengthens throughout the first 40 years, even as SO<sub>2</sub> emissions ramp-down from year 30 onwards. There is positive OHT convergence between 35°N and 60°N, consistent with the lagged SPNA surface (fig. 3). The OHT anomalies also exhibit strong latitudinal coherence in both models (i.e. anomalies appearing at all latitudes at once, with no clear lag between different 225 latitudes). The magnitude of OHT anomalies are greater in the MM model compared to LL, which is consistent with the stronger warm subpolar North Atlantic SST anomalies in MM.

Figure 6 shows a side-by-side comparison of the AMOC response between the AMOC in depth space (AMOC-depth) and the AMOC in density space (AMOC-sigma) for the two models. The AMOC-depth in both models show a strengthening across all depth levels at any given latitude. The depth of the largest anomalies is also about 500m deeper than where the mean 230 state is at its maximum. In contrast to depth space, AMOC-sigma does not show strengthening across all density classes in the subpolar latitudes (fig. 6). Between 45°N to 60°N, AMOC-sigma anomalies show a dipole pattern, negative anomalies in the lighter northward flowing waters and positive anomalies in the denser southward flowing waters. Furthermore, the largest positive anomalies are at the density class of 27.8 kg/m<sup>3</sup>, which is a denser class than where the maximum mean AMOC-sigma



strength is in the PI control ( $27.6 \text{ kg/m}^3$ ). This dipole pattern indicates that the AMOC does not uniformly strengthen across 235 all density classes, instead, the AMOC appears to have shifted to a higher density class as it strengthens. This shift of density class as the AMOC strengthens has also been found in the CESM's (Community Earth System Model) preindustrial control simulation (Yeager et al., 2021).

The AMOC-sigma is also a better representation of overturning at higher latitudes. Between  $60^\circ\text{N}$  and  $75^\circ\text{N}$ , there is also a hint of overturning shifting to higher density classes in both models. However, these high-latitude positive anomalies are very 240 weak and do not appear to be clearly connected to the positive AMOC anomalies further south, suggesting that water mass transformation over the GIN Seas and transport of dense overflow waters are likely not a major driver of the wider AMOC strengthening.

In contrast to a previous study based on multi-model ensembles of CMIP6 historical simulations (Robson et al., 2022), the difference in the AMOC response is not correlated with the size of the aerosol-induced interhemispheric imbalance. In Robson 245 et al. (2022) AMOC is highly correlated with the magnitude of energy imbalance (correlation coefficient of 0.8). However, in this set of idealised experiment, the medium resolution has a stronger AMOC response, despite a weaker interhemispheric energy imbalance of  $0.25\text{W/m}^2$  (fig. 1i). To explain the differences between the resolutions, we will investigate two different processes in the next subsections. First we will look at the differences in local surface buoyancy forcing, then the potential role for slower feedback by looking at how the spatial pattern of density anomalies evolve.

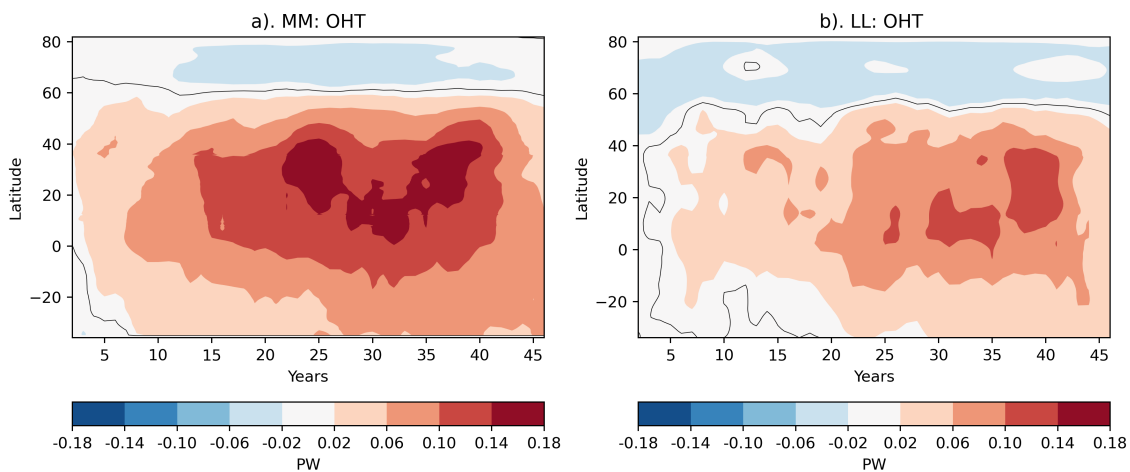


**Figure 5.** Hovmöller plot of northward OHT anomalies in the North Atlantic basin. Hovmöller diagrams of annual-mean, ensemble-mean anomalies of ocean heat transport (OHT) by latitude and time. Panels a). shows the MM model and panel b). shows the LL model. All variables are smoothed by a 5-year running mean. All shaded regions are significant at the 10% level based on a two-tailed Student's t-test. Stippling is left out for clarity.

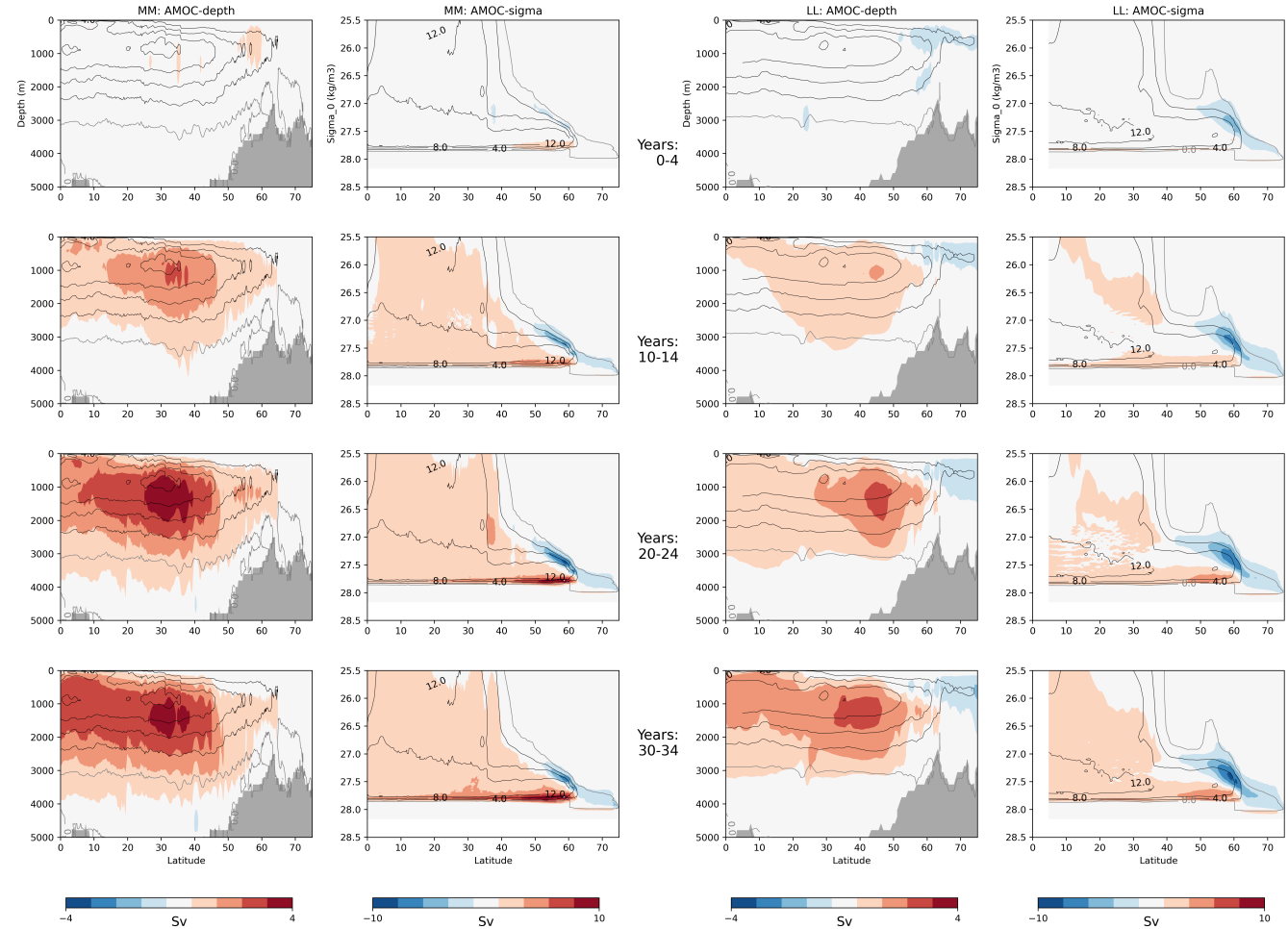


**Figure 6.** Evolution of the annual-mean, ensemble-mean anomalies of the AMOC streamfunction represented in density space (AMOC-sigma) and in depth space (AMOC-depth). The contour lines show the mean state of the pre-industrial control simulations, starting with 0 Sv represented by the grey line. Each subsequent contour has a spacing of 4 Sv. All variables are smoothed by a 5-year running mean. The MM model is shown on the left and the LL model is shown on the right. All shaded regions are significant at the 10% level, based on a two-tailed Student's t-test. Stippling is left out for clarity to show both the mean state as contour and anomalies in shading.

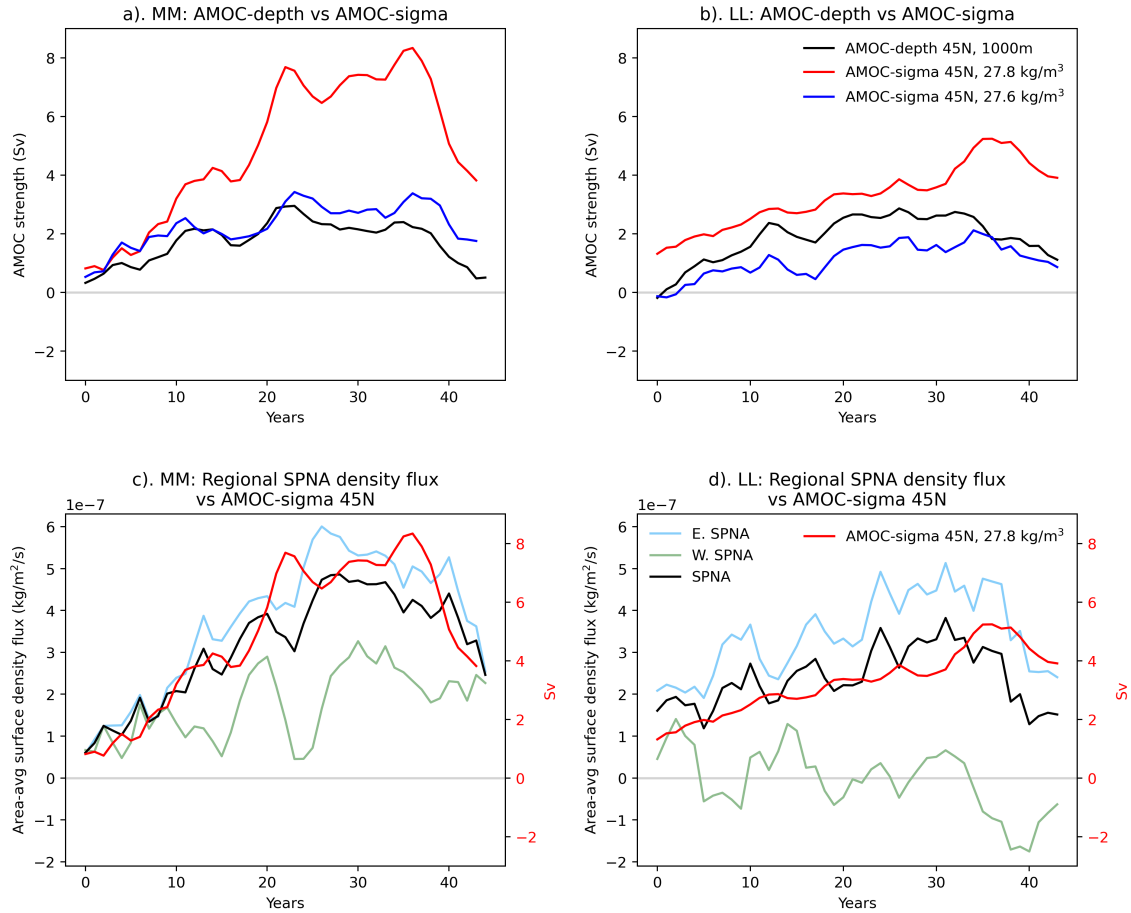


**Figure 7.** Panels a). and b). show the time series of the anomalous AMOC strength at  $45^{\circ}\text{N}$ , at depth of 1000m (AMOC-depth  $45^{\circ}\text{N}$ , blue), the timeseries of the maximum anomaly of the AMOC in density space at  $45^{\circ}\text{N}$  (AMOC-sigma  $45^{\circ}\text{N}$ ) at density of  $27.8 \text{ kg/m}^3$  (red), and AMOC-sigma  $45^{\circ}\text{N}$  at density of  $27.6 \text{ kg/m}^3$  (blue), for the MM and LL models respectively. Panels c). and d). show the time series of annual-mean anomalies of area-averaged surface density fluxes across the subpolar North Atlantic (SPNA, black) and contributions from the eastern (blue) and western (green) portion of the SPNA for the N216 and N96 models respectively. The SPNA region is defined as  $(45^{\circ}\text{N}-65^{\circ}\text{N}, 65^{\circ}\text{W}-0^{\circ}\text{W})$  and shown by black box in figure 9. The eastern and western portions are separated at Cape Farewell, shown by grey dashed line in figure 9. All variables are smoothed by a 5-year running mean.



250 **2.4 Differences in surface buoyancy forcing?**

The water mass transformation framework can be used to understand how aerosol-forced surface fluxes lead to AMOC changes (Desbruyères et al., 2019; Groeskamp et al., 2019). This framework is based on an understanding of the AMOC as a system where volume transport is in thermodynamic balance with surface water mass transformation. In the absence of mixing, the diapycnal (i.e. across density level) volume flux associated with the AMOC above a certain density level and at a specific 255 latitude, is related to the amount of air-sea exchanges of buoyancy within regions where this particular density level (isopycnal) outcrops at the surface, and north of this specific latitude. In other words, the AMOC-sigma index (i.e. AMOC strength at a particular class of density), should be proportional to the magnitude of surface fluxes over where the key isopycnal outcrops to the surface. Therefore, this subsection will first define an AMOC-sigma index and then estimate the magnitude of surface dense water formation.

260 **2.4.1 AMOC-sigma index**

Figure 7a & b shows timeseries comparison of the standard AMOC-z index (defined at a depth of 1000m, where the mean state is at maximum) and the AMOC-sigma index at density of 27.8 kg/m<sup>3</sup> and 27.6 kg/m<sup>3</sup>, at latitude of 45°N, for the 2 different resolutions. The two density levels are chosen to correspond with where the mean state and where the standard deviation is largest respectively (fig.6). 45°N is chosen as the latitude to define the AMOC index, as it is the southern boundary of 265 the western SPG and captures the water masses formed north of this latitude (Groeskamp et al., 2019) while minimising the influence of other model-dependent processes such as the southward propagation pathways of water masses (Ortega et al., 2020).

The AMOC in depth space is not a good representation for this analysis because the same depth can contain waters of many different density classes due to the E-W density gradient at high latitudes. Indeed The maximum AMOC-depth 45°N anomaly 270 is 2.95 Sv in the MM model and 2.86 Sv in the LL model (fig. 7a & b). There is also a larger difference between the AMOC-depth and AMOC-sigma index in the MM model which is consistent with differences in the simulated AMOC structure related to model resolution. Higher resolution models tend to have a stronger E-W density gradient at high-latitudes, therefore there is stronger cancellation between the light, northward flow and dense, return flow at the subpolar latitudes when represented in depth space (Hirschi et al., 2020). AMOC in density space tends to be a better representation for assessing the dynamics.

275 In density space, both indices at 27.8 kg/m<sup>3</sup> and 27.6 kg/m<sup>3</sup> capture a larger increase in the MM model (fig. 7a & b). Although the magnitude of the AMOC-sigma anomalies and the inter-model differences are much more pronounced with the 27.8 kg/m<sup>3</sup> index. The 27.8 kg/m<sup>3</sup> index has maximum anomaly of 7.89 Sv in MM and 5.24 Sv in LL, which is an increase of 52% and 42% over the maximum AMOC-sigma strength at 45°N in the PI control mean state for the MM and LL models respectively. Whereas, the 27.6 kg/m<sup>3</sup> index has maximum anomaly of 4.09 Sv and 2.94 Sv in MM and LL respectively, 280 corresponding to an increase of 30% and 26% from the maximum PI control mean. As shown in the previous section, the AMOC tends to shift to a higher density class as it strengthens, and we are interested in the difference in the AMOC response



between the two resolutions, therefore we will use the AMOC strength at the denser level of  $27.8 \text{ kg/m}^3$  as the AMOC-sigma index hereafter.

#### 2.4.2 Surface density flux

285 The combined effect of air-sea exchanges of heat and freshwater on sea water density (i.e. surface density flux) can be written as a function of the net surface heat ( $Q$ ) and freshwater ( $F$ ) fluxes as follows:

$$f = -\frac{\alpha}{C_p}Q - \beta \frac{S}{1-S}F \quad (1)$$

290 where  $\alpha$  and  $\beta$  are the (positive) thermal expansion and haline contraction coefficients,  $C_p$  is the specific heat capacity of seawater,  $S$  is the sea surface salinity (Speer and Tziperman, 1992). The sign convention used here is that positive (red) denotes an increase in sea surface density and negative (blue) denote a more buoyant sea surface.

Figure 8 shows the evolution of annual mean surface density flux anomalies alongside its decomposition into the thermal and haline components, i.e. the two terms on the right hand side of equation 1. Additionally, extended late winter (January–February–March–April, JFMA) ocean surface density  $27.6 \text{ kg/m}^3$  and  $27.8 \text{ kg/m}^3$  are highlighted by the black and blue contour lines as these density levels correspond to the maximum AMOC-sigma mean in the PI control and location of the largest AMOC-sigma anomalies in the idealised experiment respectively. The regions bounded by these contour lines indicate where these isopycnals outcrop to the surface, and therefore, the regions where surface forcing is directly driving the AMOC lower limb. The JFMA period is chosen because this is when the ocean surface is at its densest, therefore it is the period at which isopycnals of the densest water classes outcrop at the surface and water mass transformation occurs. Note that the surface density shown is the ensemble mean, not anomalies with respect to the PI control. This is because the absolute values of density are important for 300 identifying specific density classes, not the relative changes. Figure 8 focuses only on the initial 19-years, to minimise the influence of the feedback from ocean circulation changes as the strengthening of AMOC and associated heat transport can also impact on the surface fluxes and water mass transformation.

We focus first on the JFMA surface density to identify where key isopycnals are outcropping at the surface. In both models, two key regions are highlighted by where the  $27.6 \text{ kg/m}^3$  density level consistently outcrops (i.e. blue contour lines, fig. 8). 305 These are the western SPNA (WSPNA) region and the Arctic region which includes the GIN and Barents Seas. Note that the location and size of the two regions do not appear to change much with the varying levels of SO<sub>2</sub> emissions. The WSPNA outcropping region is larger in the MM model, spanning across much of both the Labrador and Irminger Seas. Whereas, in LL, the WSPNA outcropping region is smaller and does not extend as far into the Labrador and Irminger Seas. Additionally, the surface is denser in the MM model, with denser waters of  $27.8 \text{ kg/m}^3$  outcropping in the central Labrador Sea, which does not 310 occur in the LL model. In the Arctic, the regions of outcropping are more comparable between the two models (fig. 8). The Arctic surface is very dense in both models, with the  $27.8 \text{ kg/m}^3$  level outcropping across the whole of the Barents Sea and much of the eastern GIN Seas.



Where key isopycnals outcrop in the WSPNA region, the surface density flux anomalies are generally positive in both models, which indicates that surface density fluxes here are responsible for driving the AMOC (fig. 8). In the central SPNA, 315 the large surface density flux anomalies are likely related to oceanic feedback, i.e. strengthening of the AMOC leads to a delayed warming of the SST, which then leads to more heat flux out of the ocean.

The relationship between surface density flux and the isopycnal outcropping region is different in the Arctic (fig. 8). Although 320 the Arctic is extremely dense with widespread outcropping, the surface density fluxes are generally negative. These negative surface flux anomalies are likely related to the growth of sea ice (fig. 3) inhibiting air-sea interactions (fig. 4), suggesting that deep water formation in the Arctic is likely not important for the aerosol-forced AMOC strengthening.

A further question here is the relative importance of surface heat versus surface freshwater fluxes in driving the overall surface density flux, as this can help narrow down the possible processes involved.

Figure 8 only shows the initial 19 years, however the thermal component dominates the total surface density fluxes throughout 325 the whole 50-year simulation in both models. The haline component is an order of magnitude smaller than the thermal component. This result rules out many potential mechanisms involving freshwater fluxes, such as precipitation changes and sea-ice driven surface salinity changes which have been proposed in previous studies, e.g. Menary et al. (2013).

Although we have shown that surface freshwater fluxes do not appear to play a big role in dense water formation, it does not 330 mean that the salinity-controlled portion of density changes are unimportant for the overall AMOC response. The northward transport of salty water as the AMOC strengthens (Menary et al. (2013)) or the southward transport of density anomalies in the Arctic (Jungclaus et al. (2005)) may also play a role in changing the ocean density. The question of whether AMOC differences are related to differences in how density anomalies propagate around the North Atlantic basin will be explored in a later section 2.5.

#### 2.4.3 Surface-forced AMOC response and role of mean state differences

The previous section defined appropriate AMOC-sigma index, and showed that the SPNA is the key region of surface density 335 flux.

Figure 7c & d shows a comparison between the the AMOC-sigma 45°N index and the timeseries of area-averaged SPNA surface density flux alongside its decomposition into contributions from the western portion (which includes the Labrador Sea only) and the eastern portion (includes the Irminger Sea and eastern SPNA), separated at Cape Farewell (regions shown by black box and dashed grey line in figure 9). Both models show a similar relationship between the AMOC- $\sigma$  strength and the 340 total SPNA density flux (i.e. a similar amount of volume flux (Sv) per unit of density flux ( $\text{kg/m}^2/\text{s}$ )). This agreement between the two models is consistent with previous studies showing that SPNA surface fluxes can strongly predict AMOC variability (Desbruyères et al., 2019). The stronger AMOC response in the MM model is also consistent with the larger density flux anomalies in the SPNA. In the LL model, the density fluxes lag AMOC from year 30, which could be due to feedback from the AMOC strengthening, where increased northward heat transport also increases the SPNA SST and hence the surface heat 345 and density fluxes.



The differences between the models are largely explained by differences in the western part of SPNA (fig. 7c & d). The trend of surface density flux is positive in the MM model, but negative in the LL model. In contrast, the trend and magnitude of the eastern portion are more comparable between the two models. The higher maximum density flux in the MM model is likely related to an AMOC feedback, where the stronger AMOC response in MM results in stronger northward ocean heat flux and hence enhanced surface heat loss and stronger density flux.

What appears to explain the differences in both the size of isopycnal outcropping regions and the Labrador Sea surface density flux is the difference in the sea ice response. Figure 9 shows the spatial pattern of the surface density flux plotted alongside the boreal winter (DJF) sea ice concentration with the  $27.6 \text{ kg/m}^3$  and  $27.8 \text{ kg/m}^3$  isopycnals overlaid as contours. Only the 5-year mean for years 24-28 is shown for brevity, however the result described below holds true for any particular years. In the MM model, positive surface density fluxes over the Labrador Sea are accompanied by minimal sea ice growth and widespread isopycnal outcropping of both the  $27.6 \text{ kg/m}^3$  and  $27.8 \text{ kg/m}^3$  density levels. In the LL model, the Labrador Sea surface density flux anomalies are strongly negative and are collocated with large positive anomalies in sea ice concentration. Sea ice growth will inhibit air-sea interaction which results in reduced surface cooling and therefore negative density flux anomalies. Furthermore, the reduced surface density fluxes over this region also likely results in more buoyant sea surface, which is consistent with the reduced area of isopycnal outcropping.

The inter-model differences in sea ice response also appear to be consistent with difference in the model's mean states in the PI-control simulations. Figure 10 shows the mean state of winter sea ice concentration (DJF SIC) and annual mean SST in the MM model minus the LL model. In the mean state of the MM model, there is less Labrador Sea ice but more sea ice in the GIN and Barents Seas. Where there is more sea ice in the mean state, there is also colder SST, which creates conditions conducive to sea ice growth. These mean state differences are consistent with the stronger Labrador Sea ice growth in LL and stronger GIN and Barents Sea ice growth in MM. Although, the sea ice differences in the GIN and Barents Seas are likely unimportant for the AMOC response to the aerosol forcing in these two models because anomalous surface density fluxes in the Arctic do not appear to play an important role for reasons discussed in section 2.3.

In summary, inter-model differences in Labrador Sea ice response appears to control the magnitude and trend of SPNA surface density fluxes, and the size of isopycnal outcropping in the SPNA. The stronger sea ice growth in LL inhibits air-sea interaction and weakens surface density fluxes while also limiting the region of isopycnal outcropping. These two factors mean the total water mass transformation is weaker in the LL model, and likely explains why the AMOC response is weaker in LL model despite stronger overall aerosol-forced hemispheric energy imbalance. Furthermore, the differences in the sea ice response is consistent with the differences in the sea ice and SST mean states between the two models. Kuhlbrodt et al. (2018) showed that these mean state differences in SST and sea ice is related to the position of the Gulf Stream and North Atlantic Current, and the associated heat transport, which is more realistic in the MM model. A separate study found that these Labrador Sea biases also explain the disagreement between the observed and simulated overturning along the OSNAP line in the HadGEM3-GC3.1 models (Petit et al., 2023).

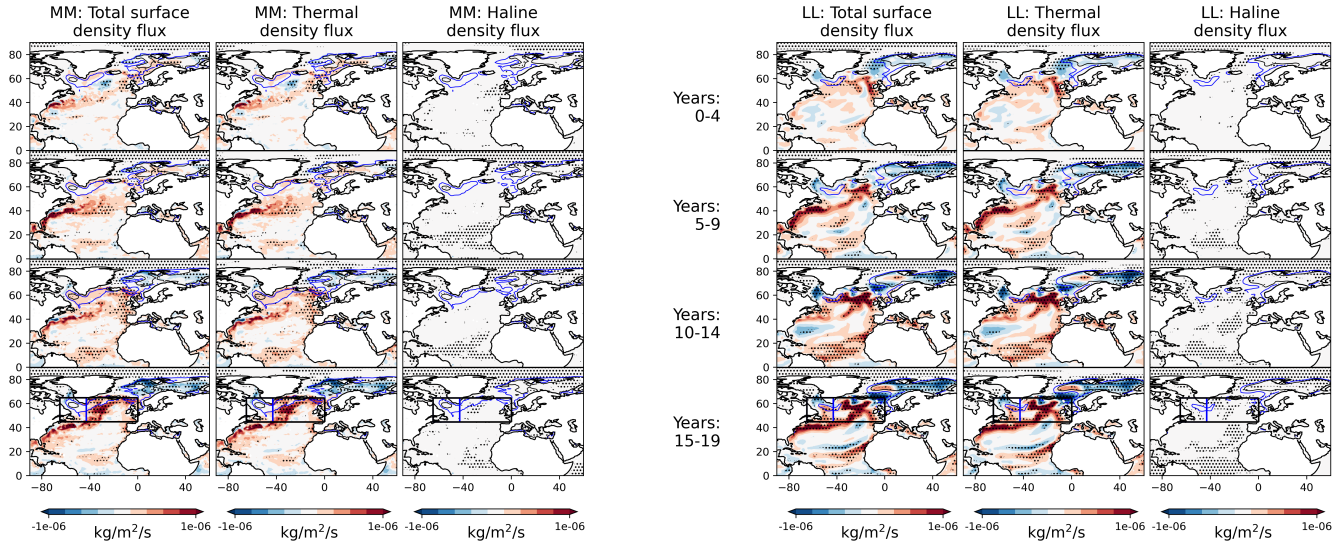


**Figure 8.** Spatial pattern and evolution of total surface density flux and its decomposition into contributions from the haline and thermal components. Contours mark areas where key isopycnals outcrop to the surface in oceanic winter. The blue and black contours regions show where the isopycnals of  $27.6 \text{ kg/m}^3$  and  $27.8 \text{ kg/m}^3$  respectively, outcrop to the surface in the extended late-winter months (January–February–March–April, JFMA). All variables are smoothed by a 5-year running mean. The MM model is shown on the left and the LL model is shown on the right. The black box in the bottom panels denote the subpolar North Atlantic (SPNA) region defined as  $(45^\circ\text{N}-65^\circ\text{N}, 65^\circ\text{W}-0^\circ\text{W})$ . Stippling indicates where the response is significant at the 10% level, based on a two-tailed Student's t-test

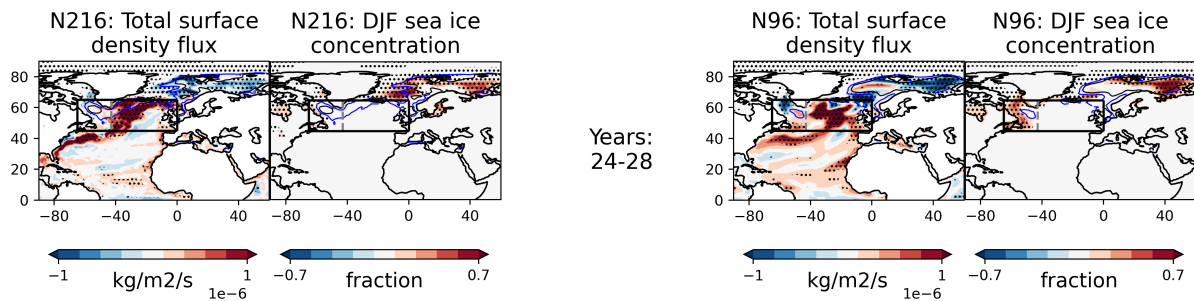


**Figure 9.** Spatial pattern of the annual-mean, ensemble-mean anomalies of surface density fluxes and December–January–February sea ice concentration (DJF SIC). All variables are smoothed by a 5-year running mean such that Years:24–28 represents the mean value between years 24 and 28. The MM model is shown on the left and the LL model is shown on the right. The blue and black contour lines represent the surface density levels of  $27.6 \text{ kg/m}^3$  and  $27.8 \text{ kg/m}^3$  respectively. The black box denotes the subpolar North Atlantic (SPNA) region. The eastern and western portions are separated at the cape of Greenland, shown by grey dashed line. Stippling indicates where the response is significant at the 10% level, based on a two-tailed Student's t-test.

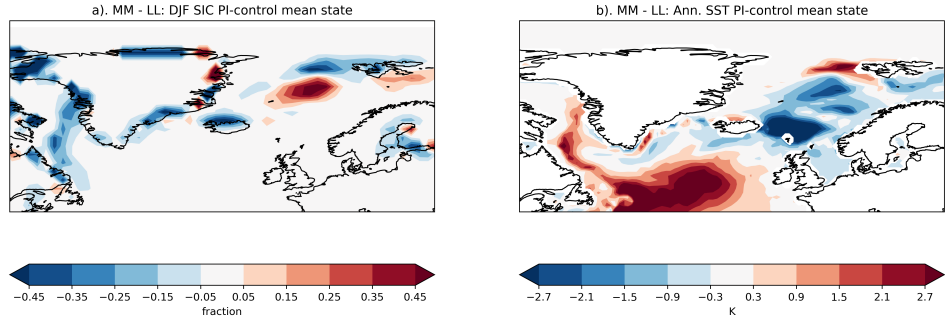


**Figure 10.** Panel (a) shows the inter-model difference (MM-LL) of the winter sea ice concentration (DJF SIC) mean state in the pre-industrial control simulations. Positive means more sea ice in the MM model and blue means less sea ice in the MM model. Panel (b) shows the inter-model difference (MM-LL) of the annual mean SST mean state in the pre-industrial control simulations.

## 2.5 Differences in propagation of density anomalies and role of salinity?

380 Local surface forcing is not the only driver of AMOC changes. Transport of density anomalies from remote surface fluxes or  
381 from ocean circulation feedback can also affect subpolar North Atlantic density and hence the AMOC (Menary et al., 2013;  
382 Vellinga and Wu, 2004; Cheng et al., 2018; Jungclaus et al., 2005). For example, Menary et al. (2013) showed that in the  
383 HadGEM2-ES model, the AMOC response to aerosol forcing is partly driven by the AMOC itself, where the strengthened  
384 AMOC contributes to the salinification of the SPNA by its increased northward transport of subtropical, salty water. Another  
385 possible mechanism involves the Arctic, Jungclaus et al. (2005) showed that changes in the East Greenland current and Den-  
386 mark Strait overflow can influence the transport of density anomalies between the Arctic and North Atlantic. This leads to our  
387 final hypothesis: Is the difference in AMOC response related to differences in how density anomalies propagate around the  
388 basin?

Figure 11 shows the evolution of upper-ocean (0-700m) density anomalies alongside the relative importance of the thermal  
390 vs the haline component. Figure 12 shows a similar diagnostic, but for the subsurface layer (1500-3000m) which corresponds  
391 to the return branch of the AMOC. The intermediate layer (700-1500m) is omitted as it mixes signal from the upper-ocean  
392 northward branch and the subsurface return branch of the AMOC. The thermal component of the ensemble mean density  
393 was calculated by using the same equation used for total density, but with time-varying ensemble mean temperature while  
394 holding the salinity at a climatological value corresponding to the first 160 years of the pre-industrial control. The full 500-year  
395 climatology was not used to avoid influence of model drift and the first 160 years cover the spread of all ensemble member's  
396 initial conditions. The haline component is calculated in a similar way to the thermal component, but with the temperature held  
397 at climatological value. The relative importance is then calculated by taking the difference between the square of the thermal

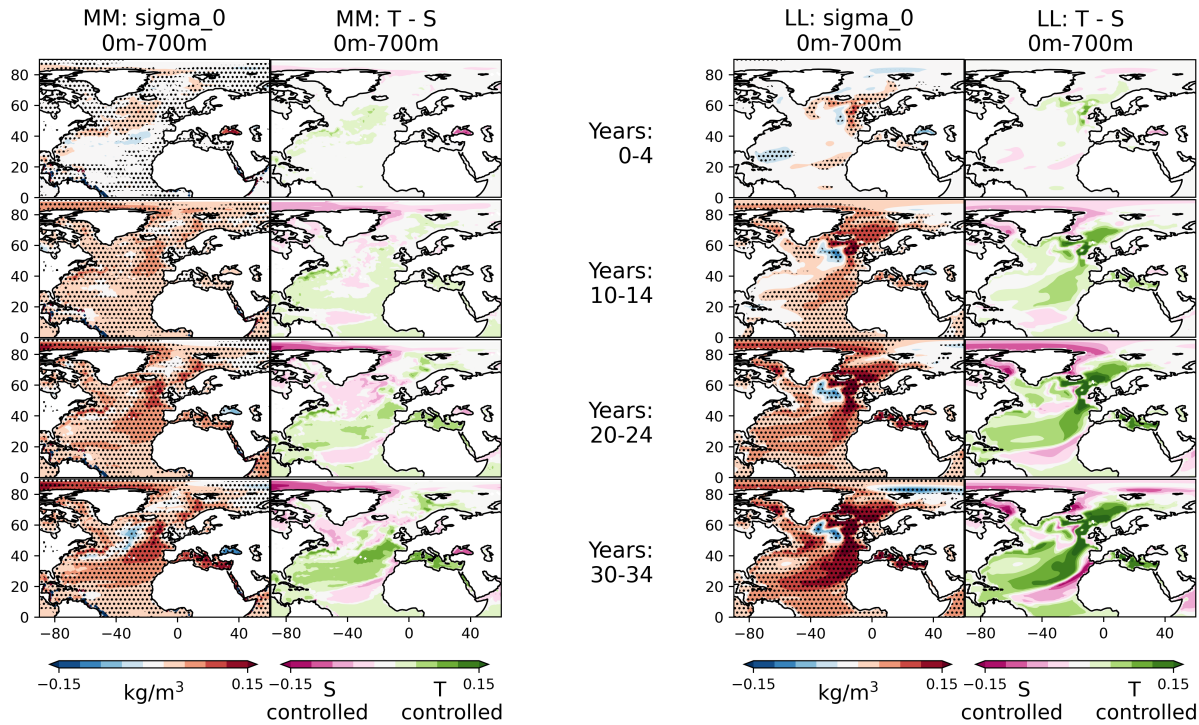


**Figure 11.** Spatial pattern and evolution of the annual-mean, ensemble-mean upper-ocean (0m-700m) potential density anomalies referenced to the ocean surface ( $\sigma_0$ ) alongside the relative importance of the thermal and haline components. Pink denotes that the density anomaly is dominated by the haline component and green denotes a thermal dominance. The MM model is shown on the left and the LL model is shown on the right. Stippling indicates where the response is significant at the 10% level, based on a two-tailed Student's t-test.

component minus the haline component, such that positive (green) denotes temperature is the dominant control on density anomalies and negative (pink) is salinity is the dominant control instead.

400 In the upper ocean, both models begin with weakly positive density anomalies in the SPNA (fig. 11). Very quickly, positive density anomalies become widespread across much of the basin, consistent with the hemisphere wide cooling (fig. 3). These positive anomalies strengthen until year 30-35, when  $\text{SO}_2$  emissions are at their maximum. However the central SPNA, the region just south of Iceland, evolves differently to the rest of the basin. In the LL model, negative anomalies appear as early as year 10-14 and strengthen until the end of the 50-year simulation. In MM, negative anomalies appear later, at year 20-24, but 405 also strengthens until the end. Decomposition of these buoyant anomalies into thermal and haline contributions show that this water mass is warm and salty (i.e. negative thermal contribution and positive haline contribution), which is a signature of the AMOC as it strengthens and transports warm salty water northwards via the Gulf Stream and North Atlantic Current (Robson et al., 2016).

410 We now turn our attention to the western and central SPNA, which includes both the Labrador and Irminger Seas, because this was identified as an important region for surface density fluxes and isopycnal outcropping, and hence AMOC variability,

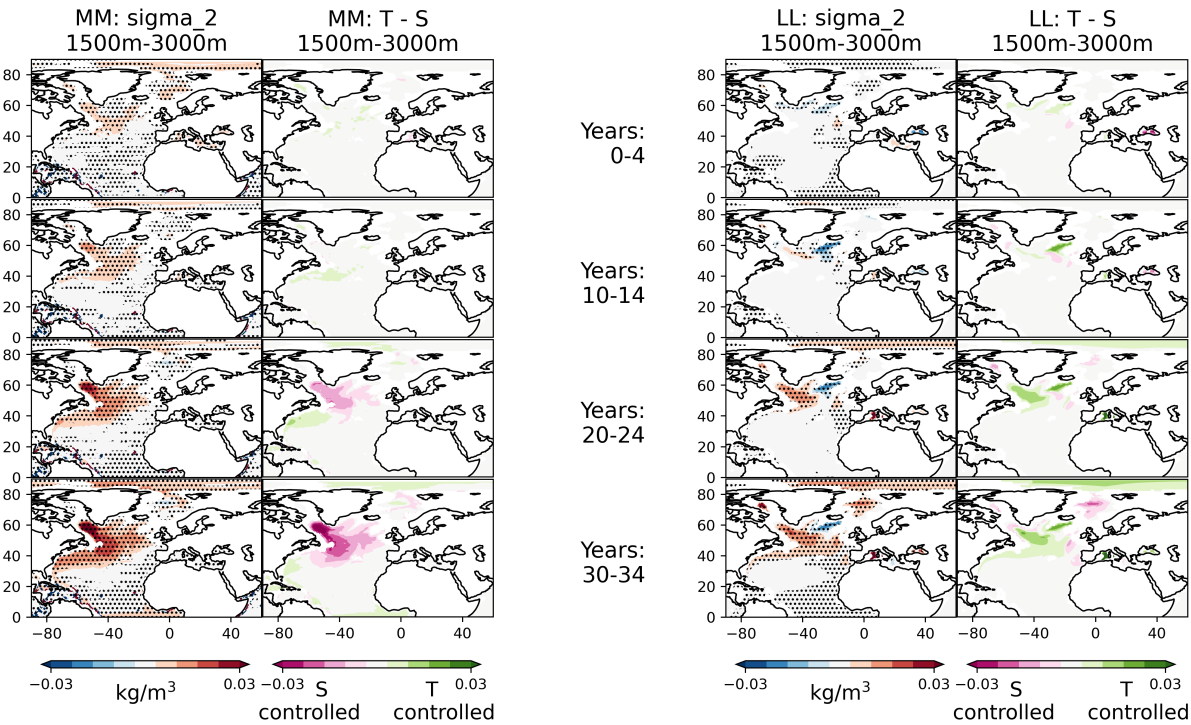


**Figure 12.** Spatial pattern and evolution of the annual-mean, ensemble-mean subsurface (1500m-3000m) potential density anomalies with respect to a reference pressure of 2000 dbar (sigma 2) alongside the relative importance of the thermal and haline components. Pink denotes that the density anomaly is dominated by the haline component and green denotes a thermal dominance. The MM model is shown on the left and the LL model is shown on the right. Stippling indicates where the response is significant at the 10% level, based on a two-tailed Student's t-test.

as discussed in section 2.4. Although both models show positive density anomalies in the Labrador Sea, the relative importance of the thermal and haline contributions differ between the models, which indicates different mechanisms. In the MM model, both the thermal and haline components weakly contribute to the positive density anomalies in the first 14 years. From years 20-24 onwards, the haline component becomes the dominant component with the thermal component becoming a negative influence instead. In the LL model, the switch from the thermal dominated to haline dominated regime occurs later, from years 30-34 onwards. In the preceding years, the thermal component positively contributes to the density anomalies while the haline component acts as a negative influence.

In the sub 1500m layer, in both models, positive density anomalies appear first in the WSPNA region and propagate southwards along the deep western boundary (fig. 12), which is a classic fingerprint of the AMOC (Buckley and Marshall, 2016).

Similar to the upper-ocean, the relative importance of the thermal and haline components is different between the models. In the MM model, the density anomalies are initially driven by both the thermal and haline components. From years 20-24 onwards, the haline component becomes the dominant driver. On the other hand, in the LL model, the overall positive subsurface



density anomalies in the western and central SPNA are largely dominated by the thermal component throughout much of the simulation. Positive haline anomalies do develop on the northern edge of the SPNA from years 30-34 onwards, but these are 425 cancelled out by negative anomalies in the thermal component.

These results show an additional difference in the mechanism driving the AMOC response between the two models. In the MM model, although the initial density anomalies in both the upper and subsurface layers of the North Atlantic are temperature-dominated, the maintenance of high density anomalies increasingly becomes salinity dominated with time. This indicates a key role in the salinification of the ocean in maintaining the strengthened AMOC. This change in the relative importance of 430 temperature and salinity also indicates that the dominant driver of the AMOC response changes through time, with surface heat fluxes dominating first and then increased salinification maintains the strengthened AMOC. Furthermore, surface water fluxes are dominated by freshening due to increased ice melt, and so is not the cause of this salinification of the North Atlantic (appendix A1). Therefore, ocean-advection is likely to be the key driver. This suggests a role for the slow salinity-advection feedback as proposed in Menary et al. (2013). In the lower resolution model, the salinification is weaker, which is consistent 435 with the weaker AMOC response and hence weaker salinity-advection feedback. Note that this feedback is likely only active when the aerosol forced cooling is strong, which removes excess heat from the AMOC strengthening and allows salinity to control density anomalies. This switch from thermal to haline-controlled dense anomalies does not occur in the unforced pre-industrial simulations Lai et al. (2022). This switch also does not occur in observations (Robson et al., 2016), which is consistent with the fact that the aerosol forced cooling is much stronger in these simulations than in the real world.

#### 440 3 Conclusions and Discussion

Idealised single-forcing experiments were performed to investigate the effect of anthropogenic SO<sub>2</sub> emissions on North Atlantic climate variability. A time-varying source of North American and European SO<sub>2</sub> emissions, representing simplified historical emissions, was introduced to otherwise pre-industrial conditions. Two versions of the HadGEM3-GC3.1 model at 445 medium (MM,  $\approx 60\text{km}$  atmosphere,  $0.25^\circ$  ocean) and low resolutions (LL,  $\approx 130\text{km}$  atmosphere,  $1^\circ$  ocean) were used to investigate the effect of model differences on the forced response. The key findings are summarised in the schematic fig. 13 and as follows:

- The idealised aerosol forcing induces a fast, wide spread SST cooling across the Northern Hemisphere and a slower, lagged warming in the subpolar North Atlantic (SPNA). The lagged SPNA warming is associated with a strengthening of the AMOC in both models, with a stronger AMOC response in the MM model compared to the LL model.
- 450 – The MM model has a stronger AMOC strengthening despite weaker aerosol-forced radiative changes, in contrast to previous studies ((Menary et al., 2020; Robson et al., 2022)). The difference in AMOC response is instead, consistent with stronger SPNA surface density fluxes (i.e. surface buoyancy forcing) and a denser sea surface (i.e. larger isopycnal outcropping area) in the MM model. These two factors indicate that there is likely stronger dense water formation in the MM model.

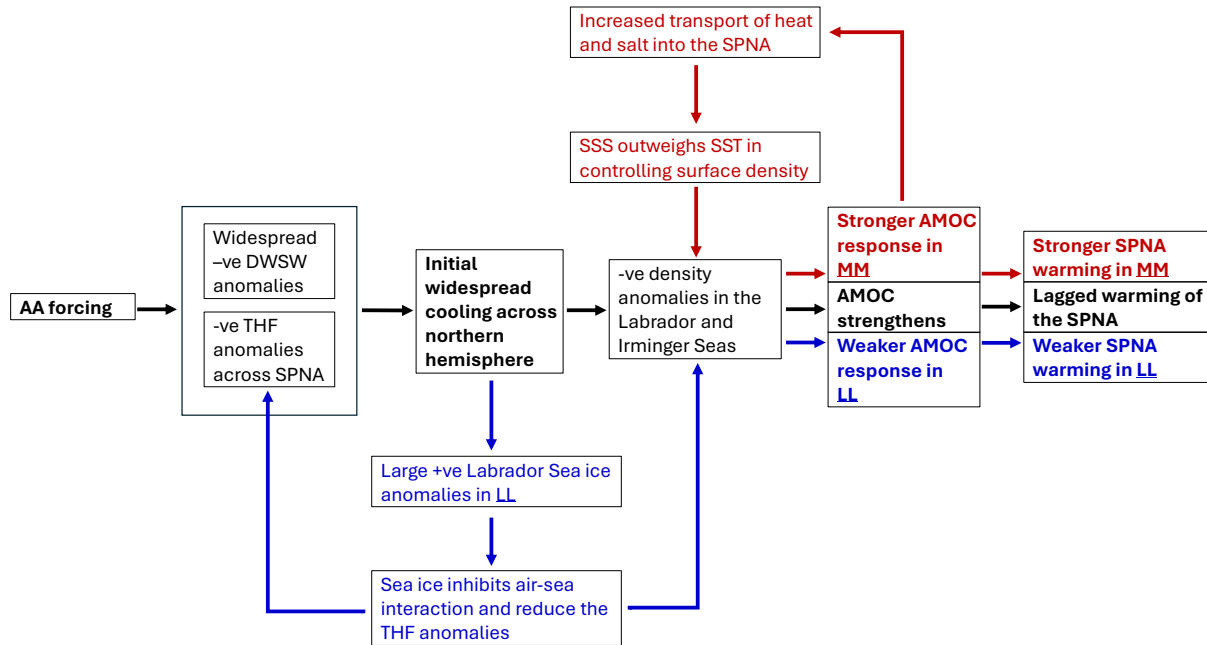


**Figure 13.** Schematic summarising the mechanism linking the idealised aerosol forcing to Atlantic SST and AMOC changes. Black arrows represent the processes common to both the medium (MM) and lower (LL) resolution models, i.e. the effect of aerosol forcing on surface heat fluxes, surface density and therefore, AMOC and SST. Red arrows represent the hypothesised salinity transport positive feedback, which is more evident in the MM model. Blue arrows represent the dampening influence of the Labrador Sea ice response, which is stronger in the LL model.

455 – Mean state differences in the Labrador Sea has a key role in determining the differences in the AMOC response to aerosol forcing. The LL model has a climatologically cooler and more sea-ice covered Labrador Sea, creating conditions favourable for more sea ice growth as the aerosol forcing cools the ocean surface. This leads to an inhibition of air-sea fluxes and a reduction in the area of isopycnal outcropping.

460 – The difference in AMOC response also appears to be related to how density anomalies propagate around the North Atlantic basin. In both models, positive surface density anomalies in the Labrador Sea changes from temperature-controlled to salinity-controlled as the AMOC strengthens. This salinity-controlled surface dense water is therefore important for sustaining the strengthened AMOC and appears to be more important in the MM model. We hypothesize that there is a positive ocean-circulation feedback at play. The AMOC is initially forced by surface density fluxes, but the increased northward transport of salty subtropical water, coupled with the ongoing aerosol-forced surface cooling, maintains high density in the SPNA and sustains the strengthened AMOC basin. The stronger AMOC response and stronger salinity-dominated density anomalies in MM are consistent with a stronger positive salt-advection feedback.



The results from this study indicates that model biases in particularly sensitive regions such as the Labrador Sea can be important for the AMOC response and hence large-scale response to anthropogenic aerosol forcing. These mean state biases have been noted in the documentation paper of the HadGEM3-GC3.1 model (Kuhlbrodt et al., 2018), which attributes the 470 difference in SST and sea ice between the MM and LL models to the position of the Gulf Stream and North Atlantic Current. The GS and NAC are too-zonal in the LL model (typical of models at this resolution) resulting in more heat being transported into the GIN Seas and less heat circulating round to the Labrador Sea.

In contrast to many other modelling studies which use multi-model ensembles to interrogate model diversity in AMV mechanisms (Robson et al., 2022; Menary et al., 2020; Wills et al., 2019; Ba et al., 2014), this study has instead focused on two very 475 similar models. An advantage to this approach is that it allows for differences in relevant processes to be attributed to specific model differences, and therefore provide additional insight which would be otherwise missed in a multimodel ensemble. An example of this is in the difference in AMOC response to AA forcing. Results in this study stand in contrast to recent analysis on CMIP6 historical simulations (Robson et al., 2022; Menary et al., 2020); we find that the magnitude of AMOC response in this set of experiments is not correlated with magnitude of the largescale aerosol forcing, instead regional differences in the 480 mean state and resulting Labrador Sea ice response appears to explain the difference in AMOC magnitude. This result indicates that although in large, multi-model ensembles, the large-scale aerosol forcing is of first-order impact in explaining differences in AMOC sensitivity (Robson et al., 2022; Menary et al., 2020), individual model differences still shape the overall response to forcing. This conclusion has implications for the operational uses of climate models, where activities such as decadal prediction, detection and attribution, or climate risk assessment, might not utilise a large ensemble of models. This uncertainty 485 highlights the need for better understanding of the impact of individual model differences on the simulated physical processes, and the need for better observations in order to understand which sets of physical processes are more realistic and thus better constrain climate models. Furthermore, the stronger AMOC response in the MM model shown in this study is consistent with previous results showing a stronger decline of the AMOC under future forcing scenarios in higher resolution models (Roberts et al., 2020).

490 A disadvantage to this approach of analysing two very similar models is that we cannot be sure whether the inter-model differences identified are robust across other models, or if they are just unique to these two models themselves. For example, the differences identified could be just a result of mean state differences, which is not only a function of model resolution, and other models of simular resolution may have different mean state biases.

Nevertheless, there are good reasons to believe that higher resolution models may lead to better representation of the North 495 Atlantic climate system. As climate models achieve increasingly higher resolutions, the representation of the dynamics become more realistic, since more processes are explicitly resolved and fewer processes have to be parameterized. More realistic representations of boundary currents and eddy transport can affect freshwater transport within the North Atlantic (Mecking et al., 2016). Higher resolution models tend to reduce surface temperature and salinity biases (Menary et al., 2015; Roberts et al., 2019) and they also tend to have stronger transport of heat and salt within the North Atlantic (Roberts et al., 2016, 2020). 500 However, the long, millennial timescale required for ocean circulations to reach equilibrium may be prohibitively expensive to run on the highest resolution models. It must also be noted that greatly increasing horizontal resolution does not always guar-



antee improvements of model biases in all regions (Petit et al., 2023; Chassignet et al., 2020), therefore progress in modelling techniques must be accompanied by progress in a process-based understanding of the effects of increasing resolution.



## Appendix A: Surface water flux components

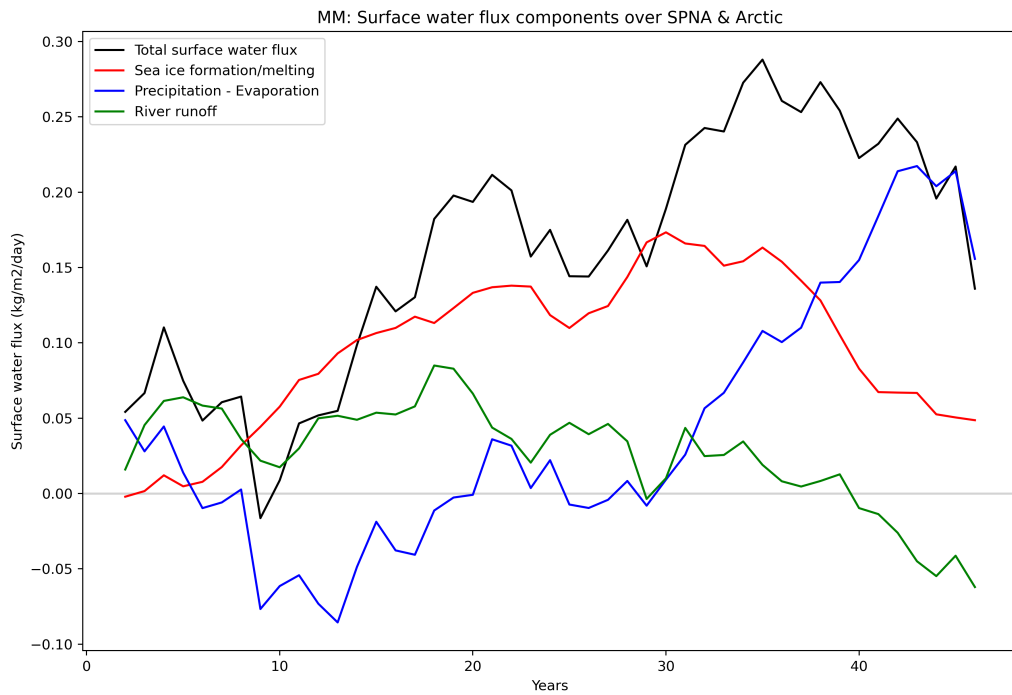


**Figure A1.** Time series of the anomalous total surface water flux (wfo, black) averaged across the Arctic and subpolar North Atlantic ( $45^{\circ}\text{N}$  to  $65^{\circ}\text{N}$ ,  $85^{\circ}\text{W}$  to  $35^{\circ}\text{E}$ ) alongside its decomposition; water flux due to sea ice melt/formation (fsitherm, red), precipitation minus evaporation (blue) and river runoff (friver, green). Positive denotes anomalous surface water flux into the ocean. Only the MM model is shown. All variables are smoothed by a 5-year running mean.

505 *Code and data availability.* The data and code used to produce the figures are available from <https://doi.org/10.5281/zenodo.15577999> (Lai et. al, 2025). These include data from the PI-control simulations and the idealised forcing experiments.

*Author contributions.* All authors conceived the study and designed the experiments and contributed to interpretation of the data. MWKL performed some model simulations, carried out the data analysis and wrote the original draft of the manuscript with input from all authors. JR, LW, ND and RS provided supervision for MWKL. JR provided directions to the data analysis and insightful commentary on the manuscript. 510 ND assisted with performing the model simulations.



*Competing interests.* Laura Wilcox is a member of the ACP editorial board.

*Acknowledgements.* MWKL was funded by a NERC-UKRI CASE studentship (2110052). JR was funded by the UKRI-NERC WISH-BONE (NE/T013516/1), SNAP-DRAGON (NE/T013494/1), CANARI (NE/W004984/1), and ALPACA (NE/Y005279/1) projects. JR was additionally funded by the UKRI (grant number 10039018) as part of the EPOC project (Explaining and Predicting the Ocean Conveyor; 515 grant number: 101059547). Views and opinions expressed are however those of the author(s) only and do not necessarily reflect those of the European Union. Neither the European Union nor the granting authority can be held responsible for them.



## References

Ba, J., Keenlyside, N. S., Latif, M., Park, W., Ding, H., Lohmann, K., Mignot, J., Menary, M., Otterå, O. H., Wouters, B., y Melia, D. S., Oka, A., Bellucci, A., and Volodin, E.: A multi-model comparison of Atlantic multidecadal variability, *Climate Dynamics*, 43, 2333–2348, 520 <https://doi.org/10.1007/s00382-014-2056-1>, 2014.

Bellomo, K., Murphy, L. N., Cane, M. A., Clement, A. C., and Polvani, L. M.: Historical forcings as main drivers of the Atlantic multidecadal variability in the CESM large ensemble, *Climate Dynamics*, 50, 3687–3698, <https://doi.org/10.1007/s00382-017-3834-3>, 2018.

Bellucci, A., Mariotti, A., and Gualdi, S.: The role of forcings in the twentieth-century North Atlantic multidecadal variability: The 1940–75 North Atlantic cooling case study, *Journal of Climate*, 30, 7317–7337, <https://doi.org/10.1175/JCLI-D-16-0301.1>, 2017.

Bjerknes, J.: Atlantic Air-Sea Interaction, 10, 1–82, [https://doi.org/10.1016/S0065-2687\(08\)60005-9](https://doi.org/10.1016/S0065-2687(08)60005-9), 1964.

Booth, B. B., Dunstone, N. J., Halloran, P. R., Andrews, T., and Bellouin, N.: Aerosols implicated as a prime driver of twentieth-century North Atlantic climate variability, *Nature*, 484, 228–232, <https://doi.org/10.1038/nature10946>, 2012.

Buckley, M. W. and Marshall, J.: Observations, inferences, and mechanisms of the Atlantic Meridional Overturning Circulation: A review, *Reviews of Geophysics*, 54, 5–63, <https://doi.org/10.1002/2015RG000493>, 2016.

Chang, C.-Y., Chiang, J. C. H., Wehner, M. F., Friedman, A. R., and Ruedy, R.: Sulfate Aerosol Control of Tropical Atlantic Climate over the Twentieth Century, *Journal of Climate*, 24, 2540 – 2555, <https://doi.org/10.1175/2010JCLI4065.1>, 2011.

Chassignet, E. P., Yeager, S. G., Fox-Kemper, B., Bozec, A., Castruccio, F., Danabasoglu, G., Horvat, C., Kim, W. M., Koldunov, N., Li, Y., Lin, P., Liu, H., Sein, D. V., Sidorenko, D., Wang, Q., and Xu, X.: Impact of horizontal resolution on global ocean–sea ice model simulations based on the experimental protocols of the Ocean Model Intercomparison Project phase 2 (OMIP-2), *Geoscientific Model Development*, 13, 4595–4637, <https://doi.org/10.5194/gmd-13-4595-2020>, 2020.

Cheng, W., Weijer, W., Kim, W. M., Danabasoglu, G., Yeager, S. G., Gent, P. R., Zhang, D., Chiang, J. C. H., and Zhang, J.: Can the Salt-Advection Feedback Be Detected in Internal Variability of the Atlantic Meridional Overturning Circulation?, *Journal of Climate*, 31, 6649 – 6667, <https://doi.org/10.1175/JCLI-D-17-0825.1>, 2018.

Cheung, A. H., Mann, M. E., Steinman, B. A., Frankcombe, L. M., England, M. H., and Miller, S. K.: Comparison of Low-Frequency Internal Climate Variability in CMIP5 Models and Observations, *Journal of Climate*, 30, 4763 – 4776, <https://doi.org/10.1175/JCLI-D-16-0712.1>, 2017.

Delworth, T. L. and Mann, M. E.: Observed and simulated multidecadal variability in the Northern Hemisphere, *Climate Dynamics*, 16, 661–676, <https://doi.org/10.1007/s003820000075>, 2000.

Desbruyères, D. G., Mercier, H., Maze, G., and Daniault, N.: Surface predictor of overturning circulation and heat content change in the 545 subpolar North Atlantic, *Ocean Science*, 15, 809–817, <https://doi.org/10.5194/os-15-809-2019>, 2019.

Eyring, V., Bony, S., Meehl, G. A., Senior, C. A., Stevens, B., Stouffer, R. J., and Taylor, K. E.: Overview of the Coupled Model Intercomparison Project Phase 6 (CMIP6) experimental design and organization, *Geoscientific Model Development*, 9, 1937–1958, <https://doi.org/10.5194/gmd-9-1937-2016>, 2016.

Gastineau, G. and Frankignoul, C.: Influence of the North Atlantic SST Variability on the Atmospheric Circulation during the Twentieth 550 Century, *Journal of Climate*, 28, 1396 – 1416, <https://doi.org/10.1175/JCLI-D-14-00424.1>, 2015.

Gillett, N. P., Shiogama, H., Funke, B., Hegerl, G., Knutti, R., Matthes, K., Santer, B. D., Stone, D., and Tebaldi, C.: The Detection and Attribution Model Intercomparison Project (DAMIP v1.0) contribution to CMIP6, *Geoscientific Model Development*, 9, 3685–3697, <https://doi.org/10.5194/gmd-9-3685-2016>, 2016.



555 Groeskamp, S., Griffies, S. M., Iudicone, D., Marsh, R., Nurser, A. G., and Zika, J. D.: The Water Mass Transformation Framework for Ocean Physics and Biogeochemistry, *Annual Review of Marine Science*, 11, 271–305, <https://doi.org/10.1146/annurev-marine-010318-095421>, pMID: 30230995, 2019.

Guo, L., Turner, A. G., and Highwood, E. J.: Local and Remote Impacts of Aerosol Species on Indian Summer Monsoon Rainfall in a GCM, *Journal of Climate*, 29, 6937 – 6955, <https://doi.org/10.1175/JCLI-D-15-0728.1>, 2016.

560 Gurvan, M., Bourdallé-Badie, R., Bouttier, P.-A., Bricaud, C., Bruciaferri, D., Calvert, D., Chanut, J., Clementi, E., Coward, A., Delrossi, D., and et al.: NEMO ocean engine, *Notes du Pôle de modélisation de l'Institut Pierre-Simon Laplace (IPSL)*, <https://doi.org/10.5281/zenodo.1472492>, 2017.

Han, Z., Luo, F., Li, S., Gao, Y., Furevik, T., and Svendsen, L.: Simulation by CMIP5 models of the atlantic multidecadal oscillation and its climate impacts, *Advances in Atmospheric Sciences*, 33, 1329–1342, <https://doi.org/10.1007/s00376-016-5270-4>, 2016.

Hassan, T., Allen, R. J., Liu, W., and Randles, C. A.: Anthropogenic aerosol forcing of the Atlantic meridional overturning circulation and 565 the associated mechanisms in CMIP6 models, *Atmospheric Chemistry and Physics*, 21, 5821–5846, <https://doi.org/10.5194/acp-21-5821-2021>, 2021.

Hirschi, J. J., Barnier, B., Böning, C., Biastoch, A., Blaker, A. T., Coward, A., Danilov, S., Drijfhout, S., Getzlaff, K., Griffies, S. M., Hasumi, H., Hewitt, H., Iovino, D., Kawasaki, T., Kiss, A. E., Koldunov, N., Marzocchi, A., Mecking, J. V., Moat, B., Molines, J. M., Myers, P. G., Penduff, T., Roberts, M., Treguier, A. M., Sein, D. V., Sidorenko, D., Small, J., Spence, P., Thompson, L. A., Weijer, W., 570 and Xu, X.: The Atlantic Meridional Overturning Circulation in High-Resolution Models, *Journal of Geophysical Research: Oceans*, 125, e2019JC015522, <https://doi.org/10.1029/2019JC015522>, 2020.

Jungclaus, J. H., Haak, H., Latif, M., and Mikolajewicz, U.: Arctic-North Atlantic interactions and multidecadal variability of the meridional overturning circulation, *Journal of Climate*, 18, 4013–4031, <https://doi.org/10.1175/JCLI3462.1>, 2005.

575 Kim, W. M., Yeager, S. G., and Danabasoglu, G.: Key Role of Internal Ocean Dynamics in Atlantic Multidecadal Variability During the Last Half Century, *Geophysical Research Letters*, 45, 13,449–13,457, <https://doi.org/10.1029/2018GL080474>, 2018.

Knight, J. R.: A signature of persistent natural thermohaline circulation cycles in observed climate, *Geophysical Research Letters*, 32, L20708, <https://doi.org/10.1029/2005GL024233>, 2005.

Kuhlbrodt, T., Jones, C. G., Sellar, A., Storkey, D., Blockley, E., Stringer, M., Hill, R., Graham, T., Ridley, J., Blaker, A., Calvert, D., 580 Copsey, D., Ellis, R., Hewitt, H., Hyder, P., Ineson, S., Mulcahy, J., Siahaan, A., and Walton, J.: The Low-Resolution Version of HadGEM3 GC3.1: Development and Evaluation for Global Climate, *Journal of Advances in Modeling Earth Systems*, 10, 2865–2888, <https://doi.org/10.1029/2018MS001370>, 2018.

Lai, W. K. M., Robson, J. I., Wilcox, L. J., and Dunstone, N.: Mechanisms of Internal Atlantic Multidecadal Variability in HadGEM3-GC3.1 at Two Different Resolutions, *Journal of Climate*, 35, 1365 – 1383, <https://doi.org/10.1175/JCLI-D-21-0281.1>, 2022.

Martin, E. R., Thorncroft, C., and Booth, B. B.: The multidecadal atlantic SST-sahel rainfall teleconnection in CMIP5 simulations, *Journal 585 of Climate*, 27, 784–806, <https://doi.org/10.1175/JCLI-D-13-00242.1>, 2014.

Mecking, J. V., Drijfhout, S. S., Jackson, L. C., and Graham, T.: Stable AMOC off state in an eddy-permitting coupled climate model, *Climate Dynamics*, 47, 2455–2470, <https://doi.org/10.1007/s00382-016-2975-0>, 2016.

Menary, M. B., Roberts, C. D., Palmer, M. D., Halloran, P. R., Jackson, L., Wood, R. A., Müller, W. A., Matei, D., and Lee, S.-K.: Mechanisms of aerosol-forced AMOC variability in a state of the art climate model, *Journal of Geophysical Research: Oceans*, 118, 2087–2096, 590 <https://doi.org/10.1002/jgrc.20178>, 2013.



Menary, M. B., Hodson, D. L. R., Robson, J. I., Sutton, R. T., Wood, R. A., and Hunt, J. A.: Exploring the impact of CMIP5 model biases on the simulation of North Atlantic decadal variability, *Geophysical Research Letters*, 42, 5926–5934, <https://doi.org/10.1002/2015GL064360>, 2015.

Menary, M. B., Robson, J., Allan, R. P., Booth, B. B. B., Cassou, C., Gastineau, G., Gregory, J., Hodson, D., Jones, C., Mignot, J., Ringer, M., Sutton, R., Wilcox, L., and Zhang, R.: Aerosol-Forced AMOC Changes in CMIP6 Historical Simulations, *Geophysical Research Letters*, 47, e2020GL088166, <https://doi.org/10.1029/2020GL088166>, 2020.

Monerie, P., Robson, J., Dong, B., Hodson, D. L. R., and Klingaman, N. P.: Effect of the Atlantic Multidecadal Variability on the Global Monsoon, *Geophysical Research Letters*, 46, 1765–1775, <https://doi.org/10.1029/2018GL080903>, 2019.

Mulcahy, J. P., Johnson, C., Jones, C. G., Povey, A. C., Scott, C. E., Sellar, A., Turnock, S. T., Woodhouse, M. T., Abraham, N. L., Andrews, M. B., Bellouin, N., Browse, J., Carslaw, K. S., Dalvi, M., Folberth, G. A., Glover, M., Grosvenor, D. P., Hardacre, C., Hill, R., Johnson, B., Jones, A., Kipling, Z., Mann, G., Molland, J., O'Connor, F. M., Palmié, J., Reddington, C., Rumbold, S. T., Richardson, M., Schutgens, N. A. J., Stier, P., Stringer, M., Tang, Y., Walton, J., Woodward, S., and Yool, A.: Description and evaluation of aerosol in UKESM1 and HadGEM3-GC3.1 CMIP6 historical simulations, *Geoscientific Model Development*, 13, 6383–6423, <https://doi.org/10.5194/gmd-13-6383-2020>, 2020.

605 Myhre, G., Forster, P. M., Samset, B. H., Hodnebrog, Ø., Sillmann, J., Aalbergsjø, S. G., Andrews, T., Boucher, O., Faluvegi, G., Fläschner, D., Iversen, T., Kasoar, M., Kharin, V., Kirkevåg, A., Lamarque, J.-F., Olivié, D., Richardson, T. B., Shindell, D., Shine, K. P., Stjern, C. W., Takemura, T., Voulgarakis, A., and Zwiers, F.: PDRMIP: A Precipitation Driver and Response Model Intercomparison Project—Protocol and Preliminary Results, *Bulletin of the American Meteorological Society*, 98, 1185 – 1198, <https://doi.org/10.1175/BAMS-D-16-0019.1>, 2017.

610 Ortega, P., Robson, J., Menary, M., Sutton, R., Blaker, A., Germe, A., Hirschi, J., Sinha, B., Hermanson, L., and Yeager, S.: Labrador Sea sub-surface density as a precursor of multi-decadal variability in the North Atlantic: a multi-model study, *Earth System Dynamics Discussions*, pp. 1–25, <https://doi.org/10.5194/esd-2020-83>, 2020.

Peings, Y. and Magnusdottir, G.: Forcing of the wintertime atmospheric circulation by the multidecadal fluctuations of the North Atlantic ocean, *Environmental Research Letters*, 9, 034 018, <https://doi.org/10.1088/1748-9326/9/3/034018>, 2014.

615 Peings, Y., Simpkins, G., and Magnusdottir, G.: Multidecadal fluctuations of the North Atlantic Ocean and feedback on the winter climate in CMIP5 control simulations, *Journal of Geophysical Research: Atmospheres*, 121, 2571–2592, <https://doi.org/https://doi.org/10.1002/2015JD024107>, 2016.

Petit, T., Robson, J., Ferreira, D., and Jackson, L. C.: Understanding the Sensitivity of the North Atlantic Subpolar Overturning in Different Resolution Versions of HadGEM3-GC3.1, *Journal of Geophysical Research: Oceans*, 128, e2023JC019672, <https://doi.org/https://doi.org/10.1029/2023JC019672>, 2023.

Rasch, P. J., Barth, M. C., Kiehl, J. T., Schwartz, S. E., and Benkovitz, C. M.: A description of the global sulfur cycle and its controlling processes in the National Center for Atmospheric Research Community Climate Model, Version 3, *Journal of Geophysical Research: Atmospheres*, 105, 1367–1385, <https://doi.org/https://doi.org/10.1029/1999JD900777>, 2000.

620 Ridley, J. K., Blockley, E. W., Keen, A. B., Rae, J. G., West, A. E., and Schroeder, D.: The sea ice model component of HadGEM3-GC3.1, *Geoscientific Model Development*, 11, 713–723, <https://doi.org/10.5194/gmd-11-713-2018>, 2018.

Roberts, M. J., Hewitt, H. T., Hyder, P., Ferreira, D., Josey, S. A., Mizielski, M., and Shelly, A.: Impact of ocean resolution on coupled air-sea fluxes and large-scale climate, *Geophysical Research Letters*, 43, 10,430–10,438, <https://doi.org/10.1002/2016GL070559>, 2016.



Roberts, M. J., Baker, A., Blockley, E. W., Calvert, D., Coward, A., Hewitt, H. T., Jackson, L. C., Kuhlbrodt, T., Mathiot, P., Roberts, C. D., Schiemann, R., Seddon, J., Vannière, B., and Vidale, P. L.: Description of the resolution hierarchy of the global coupled HadGEM3-GC3.1 model as used in CMIP6 HighResMIP experiments, *Geoscientific Model Development*, 12, 4999–5028, <https://doi.org/10.5194/gmd-12-4999-2019>, 2019.

630

Roberts, M. J., Jackson, L. C., Roberts, C. D., Meccia, V., Docquier, D., Koenigk, T., Ortega, P., Moreno-Chamarro, E., Bellucci, A., Coward, A., Drijfhout, S., Exarchou, E., Gutjahr, O., Hewitt, H., Iovino, D., Lohmann, K., Putrasahan, D., Schiemann, R., Seddon, J., Terray, L., Xu, X., Zhang, Q., Chang, P., Yeager, S. G., Castruccio, F. S., Zhang, S., and Wu, L.: Sensitivity of the Atlantic Meridional Overturning Circulation to Model Resolution in CMIP6 HighResMIP Simulations and Implications for Future Changes, *Journal of Advances in Modeling Earth Systems*, 12, e2019MS002014, <https://doi.org/10.1029/2019MS002014>, 2020.

635

Robson, J., Ortega, P., and Sutton, R.: A reversal of climatic trends in the North Atlantic since 2005, *Nature Geoscience*, 9, 513–517, <https://doi.org/10.1038/ngeo2727>, 2016.

640

Robson, J., Menary, M. B., Sutton, R. T., Mecking, J., Gregory, J. M., Jones, C., Sinha, B., Stevens, D. P., and Wilcox, L. J.: The role of anthropogenic aerosol forcing in the 1850–1985 strengthening of the AMOC in CMIP6 historical simulations, *Journal of Climate*, pp. 1 – 48, <https://doi.org/10.1175/JCLI-D-22-0124.1>, 2022.

Ruprich-Robert, Y., Msadek, R., Castruccio, F., Yeager, S., Delworth, T., and Danabasoglu, G.: Assessing the climate impacts of the observed atlantic multidecadal variability using the GFDL CM2.1 and NCAR CESM1 global coupled models, *Journal of Climate*, 30, 2785–2810, <https://doi.org/10.1175/JCLI-D-16-0127.1>, 2017.

645

Ruprich-Robert, Y., Delworth, T., Msadek, R., Castruccio, F., Yeager, S., and Danabasoglu, G.: Impacts of the Atlantic multidecadal variability on North American summer climate and heat waves, *Journal of Climate*, 31, 3679–3700, <https://doi.org/10.1175/JCLI-D-17-0270.1>, 2018.

Speer, K. and Tziperman, E.: Rates of Water Mass Formation in the North Atlantic Ocean, *Journal of Physical Oceanography*, 22, 93 – 104, 1992.

650

Storkey, D., Blaker, A. T., Mathiot, P., Megann, A., Aksenov, Y., Blockley, E. W., Calvert, D., Graham, T., Hewitt, H. T., Hyder, P., Kuhlbrodt, T., Rae, J. G. L., and Sinha, B.: UK Global Ocean GO6 and GO7: a traceable hierarchy of model resolutions, *Geoscientific Model Development*, 11, 3187–3213, <https://doi.org/10.5194/gmd-11-3187-2018>, 2018.

Sutton, R. T. and Dong, B.: Atlantic Ocean influence on a shift in European climate in the 1990s, *Nature Geoscience*, 5, 788–792, <https://doi.org/10.1038/ngeo1595>, 2012.

655

Sutton, R. T. and Hodson, D. L.: Ocean science: Atlantic Ocean forcing of North American and European summer climate, *Science*, 309, 115–118, <https://doi.org/10.1126/science.1109496>, 2005.

Sutton, R. T., McCarthy, G. D., Robson, J., Sinha, B., Archibald, A. T., and Gray, L. J.: Atlantic multidecadal variability and the U.K. acsis program, *Bulletin of the American Meteorological Society*, 99, 415–425, <https://doi.org/10.1175/BAMS-D-16-0266.1>, 2018.

660

Thornhill, G. D., Collins, W. J., Kramer, R. J., Olivié, D., Skeie, R. B., O'Connor, F. M., Abraham, N. L., Checa-Garcia, R., Bauer, S. E., Deushi, M., Emmons, L. K., Forster, P. M., Horowitz, L. W., Johnson, B., Keeble, J., Lamarque, J.-F., Michou, M., Mills, M. J., Mulcahy, J. P., Myhre, G., Nabat, P., Naik, V., Oshima, N., Schulz, M., Smith, C. J., Takemura, T., Tilmes, S., Wu, T., Zeng, G., and Zhang, J.: Effective radiative forcing from emissions of reactive gases and aerosols – a multi-model comparison, *Atmospheric Chemistry and Physics*, 21, 853–874, <https://doi.org/10.5194/acp-21-853-2021>, 2021.

Twomey, S.: The Influence of Pollution on the Shortwave Albedo of Clouds, *Journal of Atmospheric Sciences*, 34, 1149 – 1152, [https://doi.org/10.1175/1520-0469\(1977\)034<1149:TIPOT>2.0.CO;2](https://doi.org/10.1175/1520-0469(1977)034<1149:TIPOT>2.0.CO;2), 1977.



Undorf, S., Bollasina, M. A., Booth, B. B. B., and Hegerl, G. C.: Contrasting the Effects of the 1850–1975 Increase in Sulphate Aerosols from North America and Europe on the Atlantic in the CESM, *Geophysical Research Letters*, 45, 11,930–11,940, <https://doi.org/10.1029/2018GL079970>, 2018.

670 Valcke, S., Craig, T., and Coquart, L.: OASIS3-MCT User Guide, OASIS3-MCT 3.0, Technical Report., TR/CMGC/15/38, CERFACS/CNRS SUC URA No. 1875, Toulouse, France,, 2015.

Vellinga, M. and Wu, P.: Low-latitude freshwater influence on centennial variability of the Atlantic thermohaline circulation, *Journal of Climate*, 17, 4498–4511, <https://doi.org/10.1175/3219.1>, 2004.

675 Walters, D., Baran, A. J., Boutle, I., Brooks, M., Earnshaw, P., Edwards, J., Furtado, K., Hill, P., Lock, A., Manners, J., Morcrette, C., Mulcahy, J., Sanchez, C., Smith, C., Stratton, R., Tennant, W., Tomassini, L., Weverberg, K. V., Vosper, S., Willett, M., Browse, J., Bushell, A., Carslaw, K., Dalvi, M., Essery, R., Gedney, N., Hardiman, S., Johnson, B., Johnson, C., Jones, A., Jones, C., Mann, G., Milton, S., Rumbold, H., Sellar, A., Ujije, M., Whitall, M., Williams, K., and Zerroukat, M.: The Met Office Unified Model Global Atmosphere 7.0/7.1 and JULES Global Land 7.0 configurations, *Geoscientific Model Development*, 12, 1909–1963, <https://doi.org/10.5194/gmd-12-1909-2019>, 2019.

680 Wang, C., Dong, S., Evan, A. T., Foltz, G. R., and Lee, S.-K.: Multidecadal Covariability of North Atlantic Sea Surface Temperature, African Dust, Sahel Rainfall, and Atlantic Hurricanes, *Journal of Climate*, 25, 5404 – 5415, <https://doi.org/10.1175/JCLI-D-11-00413.1>, 2012.

Watanabe, M. and Tatebe, H.: Reconciling roles of sulphate aerosol forcing and internal variability in Atlantic multidecadal climate changes, *Climate Dynamics*, 53, 4651–4665, <https://doi.org/10.1007/s00382-019-04811-3>, 2019.

685 Wilcox, L. J., Dunstone, N., Lewinschal, A., Bollasina, M., Ekman, A. M. L., and Highwood, E. J.: Mechanisms for a remote response to Asian anthropogenic aerosol in boreal winter, *Atmospheric Chemistry and Physics*, 19, 9081–9095, <https://doi.org/10.5194/acp-19-9081-2019>, 2019.

690 Williams, K. D., Copsey, D., Blockley, E. W., Bodas-Salcedo, A., Calvert, D., Comer, R., Davis, P., Graham, T., Hewitt, H. T., Hill, R., Hyder, P., Ineson, S., Johns, T. C., Keen, A. B., Lee, R. W., Megann, A., Milton, S. F., Rae, J. G. L., Roberts, M. J., Scaife, A. A., Schiemann, R., Storkey, D., Thorpe, L., Watterson, I. G., Walters, D. N., West, A., Wood, R. A., Woollings, T., and Xavier, P. K.: The Met Office Global Coupled Model 3.0 and 3.1 (GC3.0 and GC3.1) Configurations, *Journal of Advances in Modeling Earth Systems*, 10, 357–380, <https://doi.org/10.1002/2017MS001115>, 2018.

Wills, R. C., Armour, K. C., Battisti, D. S., and Hartmann, D. L.: Ocean-atmosphere dynamical coupling fundamental to the atlantic multidecadal oscillation, *Journal of Climate*, 32, 251–272, <https://doi.org/10.1175/JCLI-D-18-0269.1>, 2019.

695 Yeager, S., Castruccio, F., Chang, P., Danabasoglu, G., Maroon, E., Small, J., Wang, H., Wu, L., and Zhang, S.: An outsized role for the Labrador Sea in the multidecadal variability of the Atlantic overturning circulation, *Science Advances*, 7, eabh3592, <https://doi.org/10.1126/sciadv.abh3592>, 2021.

Zhang, R. and Delworth, T. L.: Impact of Atlantic multidecadal oscillations on India/Sahel rainfall and Atlantic hurricanes, *Geophysical Research Letters*, 33, <https://doi.org/https://doi.org/10.1029/2006GL026267>, 2006.

700 Zhang, R., Delworth, T. L., Sutton, R., Hodson, D. L. R., Dixon, K. W., Held, I. M., Kushnir, Y., Marshall, J., Ming, Y., Msadek, R., Robson, J., Rosati, A. J., Ting, M., and Vecchi, G. A.: Have Aerosols Caused the Observed Atlantic Multidecadal Variability?, *Journal of the Atmospheric Sciences*, 70, 1135 – 1144, <https://doi.org/10.1175/JAS-D-12-0331.1>, 2013.